

# Direct numerical simulation of turbulent open channel flows at moderately high Reynolds numbers

Jie Yao<sup>1,†</sup>, Xi Chen<sup>2</sup> and Fazle Hussain<sup>1</sup>

<sup>1</sup>Department of Mechanical Engineering, Texas Tech University, Lubbock, TX 79409, USA

<sup>2</sup>Key Laboratory of Fluid Mechanics of Ministry of Education, Beijing University of Aeronautics and Astronautics, Beijing 100191, PR China

(Received 11 May 2022; revised 8 September 2022; accepted 7 November 2022)

Well-resolved direct numerical simulations of turbulent open channel flows (OCFs) are performed for friction Reynolds numbers up to  $Re_\tau = 2000$ . Various turbulent statistics are documented and compared with the closed channel flows (CCFs). As expected, the mean velocity profiles of the OCFs match well with the CCFs in the near-wall region but diverge notably in the outer region. Interestingly, a logarithmic layer with Kármán constant  $\kappa = 0.363$  occurs for OCF at  $Re_\tau = 2000$ , distinctly different from CCF. Except for a very thin layer near the free surface, most of the velocity and vorticity variances match between OCFs and CCFs. The one-dimensional energy spectra reveal that the very-large-scale motions (VLSMs) with streamwise wavelength  $\lambda_x > 3h$  or spanwise wavelength  $\lambda_z > 0.5h$  contribute the most to turbulence intensity and Reynolds shear stress in the overlap and outer layers (where  $h$  is the water depth). Furthermore, the VLSMs in OCFs are stronger than those in CCFs, resulting in a slightly higher streamwise velocity variance in the former. Due to the footprint effect, these structures also have significant contributions to the mean wall shear stress, and the difference between OCF and CCF enlarges with increasing  $Re_\tau$ . In summary, the free surface in OCFs plays an essential role in various flow phenomena, including the formation of stronger VLSMs and turbulent kinetic energy redistribution.

**Key words:** turbulent boundary layers, channel flow

## 1. Introduction

Turbulent flows over solid surfaces (i.e. wall turbulence) is of great importance in engineering applications. Turbulent plane channel flows with impermeable no-slip walls

† Email address for correspondence: [jie.yao@ttu.edu](mailto:jie.yao@ttu.edu)

© The Author(s), 2022. Published by Cambridge University Press. This is an Open Access article, distributed under the terms of the Creative Commons Attribution licence (<http://creativecommons.org/licenses/by/4.0/>), which permits unrestricted re-use, distribution and reproduction, provided the original article is properly cited.

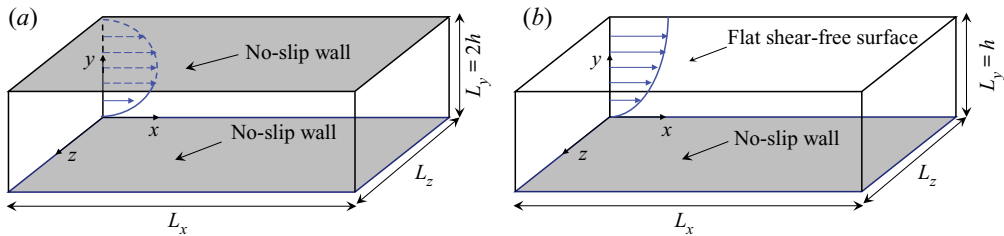


Figure 1. Schematic of the flow configuration: (a) closed channel flow and (b) open channel flow. Here  $L_x$ ,  $L_y$  and  $L_z$  are the computational domain size in the streamwise ( $x$ ), wall-normal ( $y$ ) and spanwise ( $z$ ) directions, respectively.

at the bottom and top (hereinafter referred to as closed channel flows, CCFs; see [figure 1a](#)) have been explored extensively over the last few decades both in experiments (Hussain & Reynolds 1975; Gubian *et al.* 2019) and numerical simulations (Kim, Moin & Moser 1987; Bernardini, Pirozzoli & Orlandi 2014; Lee & Moser 2015; Hoyas *et al.* 2022). Another important type of wall turbulence is open channel flows (OCFs) in which one of the no-slip walls is replaced by a free-slip boundary condition ([figure 1b](#)). The OCF is of practical relevance to many civil engineering applications, such as river, lake and ocean flows (Calmet & Magnaudet 2003; Nezu 2005; Chaudhry 2007). During the past decades, significant attention has been given to the study of the OCFs, concerning various aspects, such as heat and mass transfer (Pinelli *et al.* 2022), sediment transportation (López & García 1998; Wu, Rodi & Wenka 2000; Khosronejad & Sotiropoulos 2014) and roughness effects (Qi *et al.* 2018; Aghaei Jouybari, Brereton & Yuan 2019).

In this study, we restrict ourselves to an idealised 2-D uniform OCF over a smooth bed. Note that a number of specific features make OCF distinctly different from other types of canonical wall turbulence, such as pipes, CCF and boundary layers. If we consider pipes and CCFs as ‘internal’ flows and boundary layers as ‘external’ flows, then the OCFs can be viewed as a flow occupying an intermediate position between them, displaying characteristics of both external and internal flows (Cameron, Nikora & Stewart 2017). Hence, a detailed comparison between OCF and other canonical wall turbulence is essential for better understanding the physics of wall turbulence: the primary goal of the current work. Most of the previous research on smooth bed OCF has been conducted experimentally (Nezu & Rodi 1986; Roussinova, Shinneeb & Balachandar 2010; Wang *et al.* 2017). However, the experiments are hampered by the technological difficulties of performing measurements very close to the wall and the free surface. Therefore, direct numerical simulation (DNS), which has many advantages over the experimental approach, has been recently employed to better understand turbulence statistics and coherent structures. However, compared with other types of wall turbulence, relatively few DNS have been performed on the configuration of OCFs, and most of them are limited to low Reynolds numbers. Lam & Banerjee (1992) carried out the first DNS of OCF with a pseudo-spectral formulation of the Navier–Stokes equations and discussed the role of interfacial shear stress on streak formation. Handler *et al.* (1993) performed a similar DNS of OCF, mainly focusing on the statistical aspects of the free-surface turbulence, such as the budget of the Reynolds stresses. They observed that the spanwise component of turbulence kinetic energy (TKE) increases with decreasing distance from the free surface. Komori *et al.* (1993) found that near the free surface, the TKE of the vertical motion is redistributed between the other two components via the pressure strain effect, causing higher stress anisotropy compared with the outer region of the canonical

turbulent boundary layer. The thickness of the anisotropic vorticity layer where the surface parallel vorticity fluctuation components rapidly drop is very thin in OCF, according to the observation by Calmet & Magnaudet (2003) via large eddy simulation.

Recent research on high-Reynolds-number wall turbulence shows numerous interesting features, such as the generation of large-scale motions (LSMs) and very-large-scale motions (VLSMs) (Kim & Adrian 1999; Balakumar & Adrian 2007; Cameron *et al.* 2017). Currently, the highest Reynolds number of DNS for OCF is  $Re_\tau \approx 600$  (Bauer 2015; Yoshimura & Fujita 2020), substantially lower than the highest in experiments by Duan *et al.* (2020) (i.e.  $Re_\tau \approx 2400$ ). Due to the absence of high-resolution DNS database, CCF data are often used as a numerical surrogate instead, as OCFs near the wall have similar characteristics as the classical wall turbulence. Approaching the free surface, in contrast, OCF differs dramatically from CCF, because Reynolds stresses become highly anisotropic in the former. Furthermore, OCFs are believed to exhibit different behaviour in terms of large-scale coherent motion when compared with other wall flows. For instance, Peruzzi *et al.* (2020) showed that the LSMs and VLSMs are detectable over a much larger wall-normal extent in OCFs, and VLSMs can arise at  $Re_\tau$  as low as 725: much lower than that normally required in other types of wall turbulence. Duan *et al.* (2020) demonstrated that the VLSMs are stronger in OCFs than in other wall flows. This difference is closely related to the phenomenon of TKE redistribution, i.e. the higher streamwise turbulence intensity near the free-surface of OCFs is directly contributed by the higher strength of VLSMs therein.

The objective of this work is to enhance our understanding of smooth bed OCFs through well-resolved DNS at reasonably high Reynolds numbers, with a particular focus on their similarity/dissimilarity with other types of canonical wall turbulence. The rest of the paper is organised as follows. Section 2 details the simulation methods and parameters, along with other simulations and experiments used for comparison. Section 3 presents the main results, including the mean velocity, Reynolds stress, vorticity fluctuations, and the contribution of VLSMs to the turbulence statistics. Finally, conclusions are drawn in § 4.

## 2. Numerical simulation

DNS of fully developed turbulent OCF (figure 1a) are performed with the pseudo-spectral code developed by Lee & Moser (2015). In this study,  $x$ ,  $y$  and  $z$  denote the streamwise, wall-normal and spanwise directions, respectively; the corresponding velocity components are  $u$ ,  $v$  and  $w$ . The incompressible Navier–Stokes equations are solved using the method of Kim *et al.* (1987), in which equations for the wall-normal vorticity and the Laplacian of the wall-normal velocity are time-advanced. In the wall-parallel (i.e.  $x$  and  $z$ ) directions, periodic boundary conditions are employed, and in the wall-normal direction, no-slip ( $u, v, w = 0$ ) and free-slip ( $du/dy, dw/dy, v = 0$ ) boundary conditions are applied at the wall and the free surface, respectively. The mesh was uniform in the wall-parallel directions, and stretched in the wall-normal direction with refinement near both the wall and free surface. A Fourier–Galerkin method is used in the streamwise and spanwise directions, whereas the wall-normal direction is represented using a seventh-order B-spline collocation method. A low-storage implicit–explicit scheme based on third-order Runge–Kutta for the nonlinear terms and Crank–Nicolson for the viscous terms are used for time advance. The flow is driven by a pressure gradient, which varies in time to ensure constant mass flux through the channel. For more details about the code, the numerical methods and how the simulations are run, see Lee, Malaya & Moser (2013); Lee & Moser (2015).





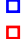


Case	$Re_\tau$	$Re_b$	$N_x \times N_y \times N_z$	$\Delta x^+$	$\Delta y_w^+$	$\Delta y_{max}^+$	$\Delta z^+$	$Ti_\tau/h$	Symbol
OCF180	182	2857	$512 \times 192 \times 512$	9.0	0.03	1.4	4.5	47	
OCF550	547	10 000	$1536 \times 384 \times 1536$	9.0	0.05	2.0	4.5	10.4	
OCF1000	1004	20 000	$2304 \times 512 \times 2304$	10.9	0.06	2.8	5.5	12.6	
OCF2000	2006	43 478	$4096 \times 768 \times 4096$	12.3	0.09	3.8	6.2	10.1	
EXP600	614	11 462	...	...	...	...	...	...	
EXP1000	1030	20 905	...	...	...	...	...	...	
EXP1900	1903	41 496	...	...	...	...	...	...	

Table 1. Details of the numerical discretisation employed for the OCF simulations. The computational box size is  $L_x \times L_y \times L_z = 8\pi h \times h \times 4\pi h$ , with  $h$  the channel height; and  $N_x$ ,  $N_y$  and  $N_z$  are the number of grid sizes in each direction. Here  $Ti_\tau/h$  is the total simulation time without transition. Cases EXP600, EXP1000 and EXP1900 denote the time-resolved particle image velocimetry (PIV) experimental data by Duan *et al.* (2020, 2021b).





Case	$Re_\tau$	$Re_b$	$N_x \times N_y \times N_z$	$\Delta x^+$	$\Delta y_w^+$	$\Delta y_{max}^+$	$\Delta z^+$	Symbol
CCF180	182	2857	$512 \times 192 \times 384$	8.9	0.01	3.1	6.0	
CCF550	544	10 000	$1536 \times 384 \times 768$	8.9	0.01	4.5	6.7	
CCF1000	998	20 000	$2304 \times 512 \times 2048$	10.9	0.02	6.1	4.6	
CCF2000	1996	43 478	$4096 \times 768 \times 3072$	12.3	0.17	7.5	6.1	

Table 2. Details of the simulation parameters for the CCF simulations by Lee & Moser (2015). The computational box size is  $L_x \times L_y \times L_z = 8\pi h \times 2h \times 3\pi h$ , with  $h$  the half channel height; and  $N_x$ ,  $N_y$  and  $N_z$  are the number of grid sizes in each direction.

DNS is conducted at four different Reynolds numbers  $Re_\tau = 180, 550, 1000$  and  $2000$ , based on the frictional velocity  $u_\tau$  and the channel height  $h$ . The computational domain size is  $L_x \times L_y \times L_z = 8\pi h \times h \times 4\pi h$ : large enough to accommodate most large-scale structures in OCFs (Pinelli *et al.* 2022). The grid sizes, resolutions and integration times used are listed in table 1. The simulations are performed with resolutions that are comparable to those used in the previous CCF simulations (e.g. Lee & Moser 2015). Time-resolved particle image velocimetry (PIV) experimental data at three Reynolds numbers ( $Re_\tau = 614, 1030$  and  $1903$ ) reported by Duan *et al.* (2020, 2021b) are also included here for comparison. To highlight the similarity/difference between OCFs and CCFs, DNS datasets for CCFs at the same Reynolds numbers by Lee & Moser (2015, 2019) are also included. Details of the simulation parameters (i.e. grid sizes and resolutions) are provided in table 2.

### 3. Results

#### 3.1. Velocity statistics

##### 3.1.1. Mean velocity profiles

Most of the previous works in OCFs focused on the inspection of the mean velocity profiles to assess whether they follow an universal logarithmic law of the wall (e.g. Finley, Phoe & Poh 1966; Nezu & Rodi 1986; Bergstrom, Tachie & Balachandar 2001; Bonakdari *et al.* 2008). Figure 2(a) shows the non-dimensionalised mean streamwise velocity profile  $U^+ (= U/u_\tau)$  for all the datasets listed in tables 1 and 2. Hereinafter, the superscript + indicates non-dimensionalisation in wall units, i.e. with kinematic viscosity  $\nu$  and friction

DNS of open channel flows

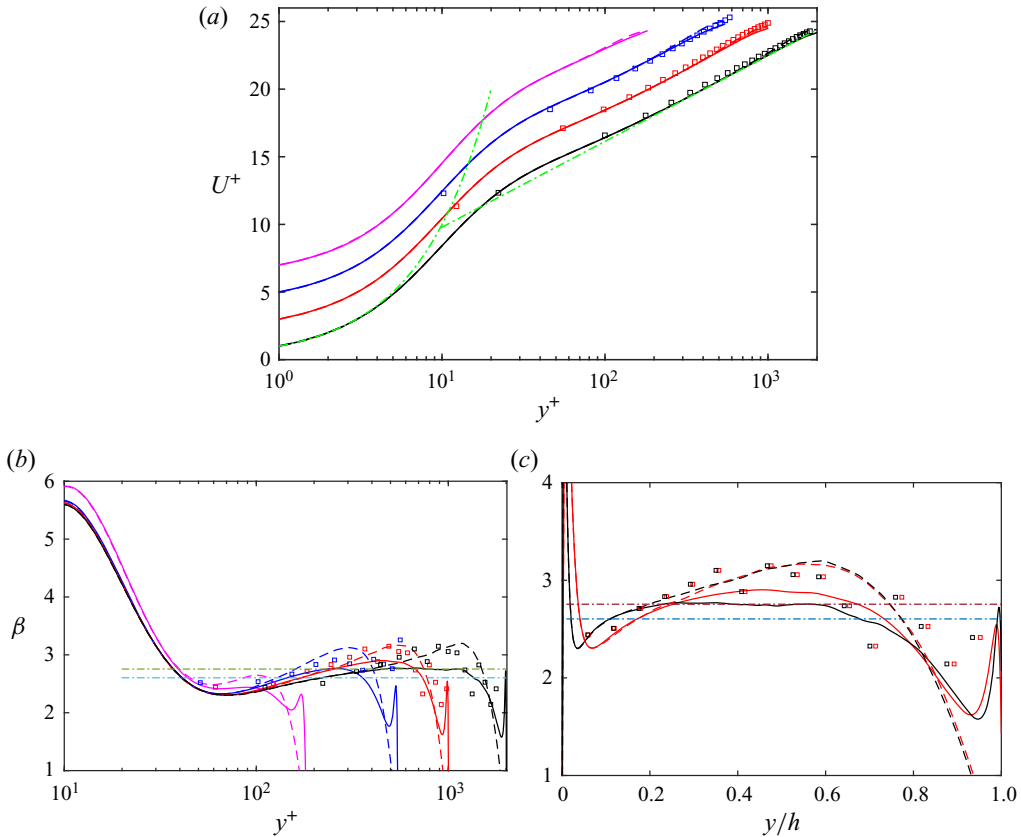


Figure 2. (a) Mean streamwise velocity and the log-law indicator function  $\beta$  in (b) wall and (c) outer units. Here, solid and dashed lines represent OCF and CCF, respectively (see tables 1 and 2 for details of the line types and symbols). In (a), each profile has been vertically shifted for better display, and the dash-dotted lines represent the law of the wall: linear law  $U^+ = y^+$  and log law  $U^+ = (1/\kappa) \ln y^+ + B$  with  $\kappa = 0.363$  and  $B = 3.45$ . In (b,c), the dash-dotted lines denote  $1/\kappa$  with  $\kappa = 0.363$  and  $0.384$  top down, respectively.

velocity  $u_\tau$ . As expected, the profiles for the OCF match well with those for CCF, with only a small discrepancy in the vicinity of the free surface, which is due to a stronger wake for the latter (Finley *et al.* 1966).

Despite extensive studies, it is still unclear whether/how the mean velocity profiles in OCF differ from other types of wall turbulence in the overlap region. Early DNS of OCF at very low  $Re_\tau$  regimes (e.g.  $Re_\tau = 134$  for Handler *et al.* (1993) and 171 for Lam & Banerjee (1992)) suggest that there is an open channel effect on the log law: either a smaller Kármán constant  $\kappa$  or smaller constant  $B$ . Later, Bauer (2015) found that both  $\kappa$  and  $B$  match well between OCF and CCF for  $Re_\tau$  up to 600. Figures 2(b) and 2(c) shows the log-law indicator function  $\beta = y^+ \partial U^+ / \partial y^+$  in inner and outer scales, respectively. It is clear that there is notable differences between OCF and CCF, particularly at the low  $Re_\tau$ , and the discrepancy in the near-wall region decreases with increasing  $Re_\tau$ . For  $Re_\tau = 2000$ , a good agreement can be observed between OCF and CCF up to  $y^+ \approx 300$ . It is consistent with that observed by Monty *et al.* (2009) for CCF, pipe and boundary layers, suggesting a near-wall universality of the inner scaled mean velocity for all types of canonical wall turbulence.

However, unlike CCF, where a constant region of  $\beta$  has not yet developed for  $Re_\tau \leq 2000$ , there is a distinct plateau for OCF, starting from  $y^+ = 500$  and extending up to  $y^+ \approx 1200$ . The experimental data of Duan *et al.* (2020) appear too noisy to confirm the existence of constant  $\beta$ . Note that high-order corrections to the log-law were sometimes introduced to better fit the mean velocity profile of CCFs at low  $Re_\tau$  in the overlap region (Afzal & Yajnik 1973; Jiménez & Moser 2007). Recent higher-Reynolds-number DNS of CCF by Lee & Moser (2015) and Hoyas *et al.* (2022) found that a constant  $\beta$  region would occur for  $Re_\tau \geq 5200$ , indicating that the minimum  $Re_\tau$  threshold for  $U^+$  to develop a logarithmic region should be lower in OCFs than in CCFs.

By fitting our OCF2000 data in the region  $500 \leq y^+ \leq 1200$ , we obtain  $\kappa = 0.363$ , which is slightly smaller than 0.384 found by Lee & Moser (2015) and 0.394 by Hoyas *et al.* (2022) for CCF. However, according to figure 2(c), the value of plateau may decrease with increasing Reynolds numbers, indicating a larger  $\kappa$  at very high  $Re_\tau$  that may eventually match with  $\kappa$  reported for CCFs. Therefore, the possibility of a universal  $\kappa$  for OCFs and CCFs as  $Re_\tau \rightarrow \infty$  cannot be excluded. If so, it will lay as strong evidence for an universal wall function (Monty *et al.* 2009). On the other hand, there is no reason to ignore the influence of outer geometry on the value of  $\kappa$ , which may indeed differ among different flows. In fact, the value of  $\kappa$  and its universality among different flow geometries are highly debated (Nagib & Chauhan 2008; She, Chen & Hussain 2017). Moreover, the current range of fitting for the value of  $\kappa$  is from  $y/h \approx 0.25$  to 0.6 for OCF2000, which is beyond the normally considered logarithmic region  $y/h \approx 0.1-0.2$  (Marusic *et al.* 2013). Hence, whether this choice is the true logarithmic range for OCF needs further study. In any case, higher  $Re_\tau$  data for OCFs are needed to clarify this significant issue.

### 3.1.2. Reynolds stresses

Figure 3 shows the normalised non-zero Reynolds stress tensor components (or velocity variances and covariances)  $\tau_{ij}^+ = \langle u'_i u'_j \rangle / u_\tau^2$ , with  $i, j = 1, 2, 3$  denoting streamwise, wall-normal and spanwise directions. Hereinafter, the velocity fluctuations are denoted using the prime symbol (e.g.  $u'$ ), and the ensemble-averaged (both in time and space) quantities of the mean velocity and velocity fluctuations are expressed using bracket (e.g.  $\langle u'v' \rangle$ ). Overall, all these quantities agree well with the CCF at the same  $Re_\tau$  in the near-wall region but differ in the outer region due to the presence of a free surface. Our DNS results differ from the experimental data EXP600, EXP1000 and EXP1900, particularly in the region close to the wall, where the experimental data have large uncertainties.

The streamwise component exhibits the well-known inner peak in the buffer layer. Consistent with other types of wall turbulence (Schlatter & Örlü 2010; Lee & Moser 2015), the location of the peak is universal with  $y_p^+ \approx 15$ , and the magnitude increases with  $Re_\tau$ , which is believed to be due to the modulation effect of LSMs and VLSMs in the logarithmic layer (Mathis, Hutchins & Marusic 2009). Interestingly, at a given  $Re_\tau$ , the peak value is slightly higher in OCF than CCF, presumably because the LSMs and VLSMs are stronger in OCF (to be discussed in § 3.2). As suggested by Townsend's attached eddy hypothesis (Townsend 1976),  $\tau_{12}^+$  and  $\tau_{22}^+$  exhibit plateaus whose extent increases with increasing  $Re_\tau$ , whereas  $\tau_{11}^+$  and  $\tau_{33}^+$  develop logarithmic regions. Similar to the CCFs, the logarithmic region of  $\tau_{11}^+$  has not yet develop for the Reynolds number considered, and  $\tau_{33}^+$  is only marginally for  $Re_\tau = 2000$ . With increasing  $Re_\tau$ , the Reynolds shear stress  $-\tau_{12}^+$  profiles also tend to become flattened and approach unity at higher  $Re_\tau$ . In addition, a good agreement on  $\tau_{12}^+$  is observed between OCFs and CCFs, even near the free surface.

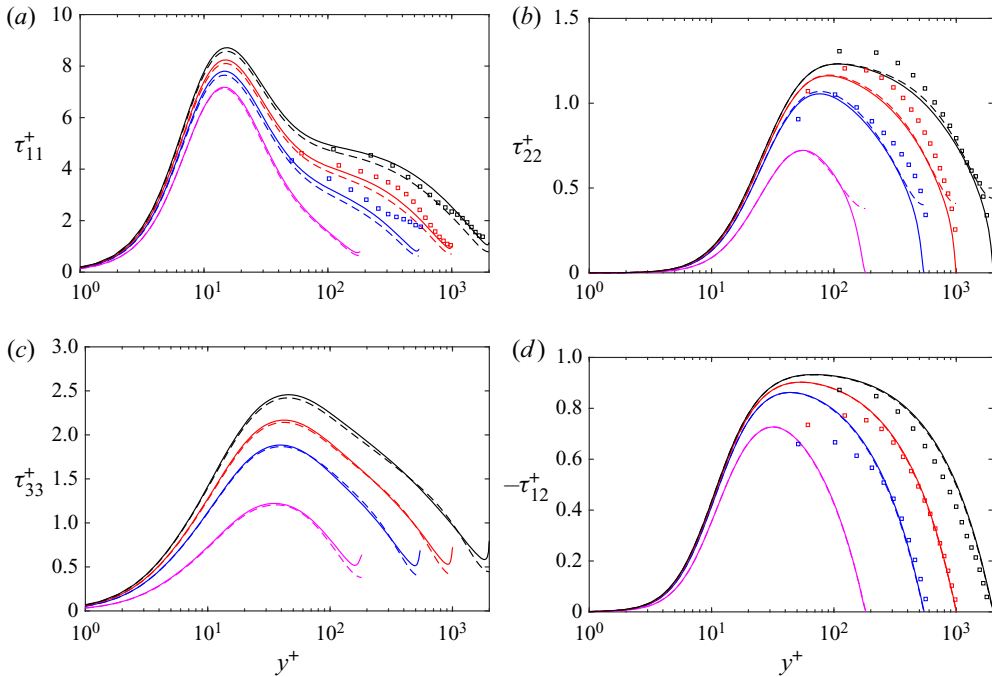


Figure 3. Reynolds stress components as a function of  $y^+$ : (a)  $\tau_{11}^+$ , (b)  $\tau_{22}^+$ , (c)  $\tau_{33}^+$  and (d)  $-\tau_{12}^+$ . The legend for line types and symbols is also given in tables 1 and 2.

This is because the asymptotic behaviour of  $\tau_{12}$  in the vicinity of the free surface should be similar to that near the centreline of CCF, both of which, in the limiting form, should follow  $\tau_{12}^+ \sim c_1(1 - y) + c_3(1 - y)^3$  with  $c_1$  and  $c_3$  the fitting coefficients (Handler *et al.* 1999).

In Chen & Sreenivasan (2021, 2022), a law of bounded dissipation is developed, which predicts a  $Re_\tau^{-1/4}$  defect power law for the averaged near-wall measures, i.e.

$$\Phi_\infty - \Phi = C_\Phi Re_\tau^{-1/4}, \tag{3.1}$$

where  $\Phi$  represents the peak of Reynolds normal stress (e.g.  $\tau_{11,p}^+$ ,  $\tau_{33,p}^+$ ), or vorticity fluctuation in the  $x$ -direction ( $\omega_{x,w}^{2+}$ ) or  $z$ -direction ( $\omega_{z,w}^{2+}$ );  $\Phi_\infty$  denotes the bounded asymptotic value, and the coefficient  $C_\Phi$  depends on the  $\Phi$  but is Reynolds number invariant. In contrast to the logarithmic growth (e.g. in Marusic, Baars & Hutchins 2017; Diaz-Daniel, Laizet & Vassilicos 2017; Samie *et al.* 2018), i.e.

$$\Phi = A \ln Re_\tau + B, \tag{3.2}$$

where  $A$  and  $B$  are parameters independent of  $Re_\tau$ , the defect power law of (3.1) supports the classical wall units scaling at asymptotically large  $Re_\tau$  because of the bounded constant  $\Phi_\infty$ . The underlying physics behind (3.1) is that the maximum turbulent production (which is exactly 1/4 after normalisation by the viscous unit  $u_\tau^4/\nu$ ) provides a bounding constraint on the dissipation rate, and, in turn, on all wall quantities and near-wall peaks in the limit of infinite Reynolds number. What matters at any finite Reynolds number is the departure of the dissipation rate from its limiting value that scales as  $u_\tau^3/\eta_o$ , where  $\eta_o$  is the Kolmogorov length scale of the outer flow. Consequently, the  $Re_\tau^{-1/4}$  scaling is obtained from the departure of the wall dissipation from its limiting value.

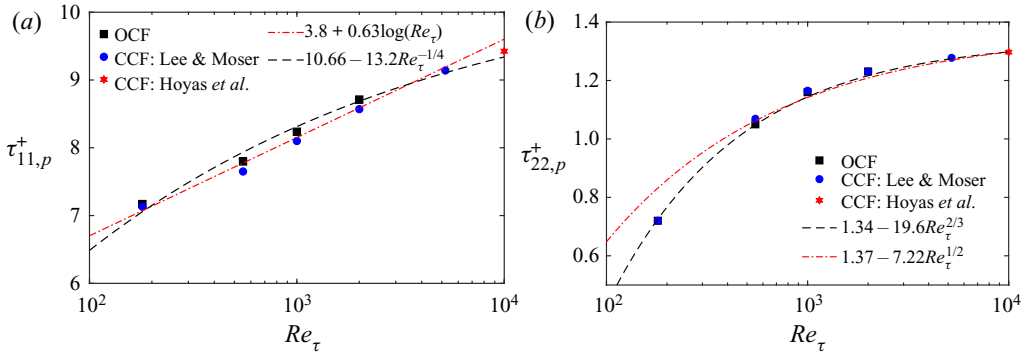


Figure 4. Variations in  $Re_\tau$  of the peak (a)  $\tau_{11,p}^+$  and (b)  $\tau_{22,p}^+$ .

Figure 4(a) shows the  $Re_\tau$ -dependence of the maximum of Reynolds normal stresses  $\tau_{11,p}^+$ , as well as the scalings of (3.1) and (3.2) with fitting parameters given in the figure legends. As a reference, DNS data of CCFs by Lee & Moser (2015) and Hoyas *et al.* (2022) are also included. The magnitude of  $\tau_{11,p}^+$  grows evidently with increasing  $Re_\tau$ . If the growth continues indefinitely with  $Re_\tau$  (as indicated by the logarithmic proposal in prior works, e.g. in Marusic *et al.* 2017), the  $\tau_{11,p}^+$  would be infinitely large and, hence, the failure of the classical wall units scaling. In contrast, (3.1) indicates a bounded  $\tau_{11,p}^+$  and, hence, the validity of the wall units scaling at asymptotically large  $Re_\tau$  (Klewicky 2022).

As noted in Chen & Sreenivasan (2022), different from  $\tau_{11}^+$  and  $\tau_{33}^+$ , the peak locations of ‘active’ motions (i.e.  $\tau_{12}^+$  and  $\tau_{22}^+$ ) extend infinitely far away from the wall (in wall units) as  $Re_\tau$  increases. Due to the Prandtl–Kármán log-law mean velocity, it is believed that the peak location  $y_{12,p}^+$  of  $\tau_{12}^+$  follows a  $Re_\tau^{1/2}$ . Chen, Hussain & She (2019) recently showed that there is a scaling transition for the peak location  $y_{12,p}^+$  of  $\tau_{12}^+$ . For low  $Re_\tau$ ,  $y_{12,p}^+$  is in the viscous buffer layer rather than in the logarithmic layer; thus, the previous derivation of the  $Re_\tau^{1/2}$  scaling is valid only for high  $Re_\tau$ . Instead, Chen *et al.* (2019) presented an alternative  $Re_\tau^{1/3}$  scaling for low  $Re_\tau$  (less than 3000) based on the peak located in the buffer layer. For  $\tau_{22}^+$ , its peak is believed to follow the scaling of  $\tau_{12}^+$  under the ‘active’ motion (Townsend 1976), which is indeed validated in figure 4(b). The peak magnitude of both OCF and CCF follows  $\tau_{22,p}^+ \approx c_0 - c_1 Re_\tau^{-2/3}$  with  $c_0 \approx 1.34$  and  $c_1 \approx 19.6$  fitted from our DNS data. One can also use the high  $Re_\tau$  scaling to fit data of  $\tau_{22,p}^+$ , i.e.  $\tau_{22,p}^+ = 1.37 - 7.22 Re_\tau^{-1/2}$  shown in figure 4(b), but this would have a larger departure at low  $Re_\tau$ .

In the outer region,  $\tau_{11}^+$  of OCFs is larger than that of CCFs, also observed by Tachie & Adane (2007). As shown in figure 5(a),  $\tau_{22}^+$  and  $\tau_{33}^+$  for CCFs at the centreline are almost identical and both slightly increase with increasing  $Re_\tau$ , in contrast to  $\tau_{11}^+$  which appears to saturate at high  $Re_\tau$  (whereas the centreline vorticities decrease with increasing  $Re_\tau$  in CCFs; see figure 5b). The trend for CCFs suggests that as  $Re_\tau$  increases, the flow near the channel centre becomes more isotropic. Due to impermeability of the free surface, the Reynolds normal stresses of OCFs are highly anisotropic when compared with the CCFs. Specifically on the free surface of OCFs, as the wall-normal Reynolds stress  $\tau_{22}^+$  drops to zero with its energy transferring to the wall-parallel components,  $\tau_{11}^+$  and  $\tau_{33}^+$  are higher than those of CCFs. Moreover, the energy of the wall-normal component is



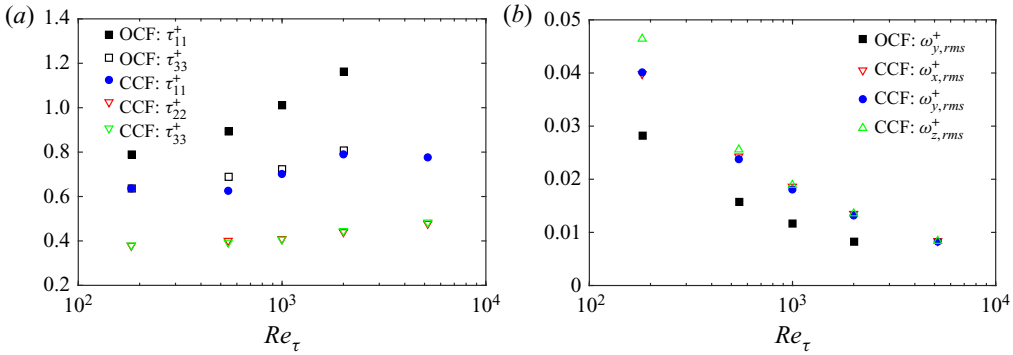


Figure 5. Variation in  $Re_\tau$  of (a) Reynolds stress and (b) root-mean-square (r.m.s.) vorticity fluctuations on the free surface for OCF and channel centreline for CCF.

almost equally transferred to the streamwise  $\tau_{11}^+$  and the spanwise  $\tau_{33}^+$  components, in agreement with that observed in Swean *et al.* (1991), Bauer (2015) and Pinelli *et al.* (2022). In addition, for the  $Re_\tau$  considered here, both  $\tau_{11}^+$  and  $\tau_{33}^+$  on the free surface rise with increasing  $Re_\tau$ , suggesting more energy transfer at higher  $Re_\tau$ . In this regard, Komori *et al.* (1993) and Handler *et al.* (1993) showed that the pressure strain and anisotropic dissipation are the main reasons for the anisotropy of Reynolds stresses. On the other hand, it would be interesting to see whether the saturation of  $\tau_{11}^+$  in CCFs at high  $Re_\tau$  similarly occurs for OCFs. If this happens, the wall-normal energy component would then be mostly transferred to the spanwise component in OCFs.

### 3.1.3. Vorticity fluctuation

The root-mean-square (r.m.s.) vorticity fluctuations (variances)  $\langle \omega_i^2 \rangle$  are examined in figure 6. When compared with CCFs, the vorticity profiles match well in the vicinity of the wall. In addition,  $\omega_{y,rms}^+$  is remarkably  $Re_\tau$ -invariant for the inner flow region, whereas both  $\omega_{x,rms}^+$  and  $\omega_{z,rms}^+$  show notable  $Re_\tau$  dependence, particularly at the wall where they reach their corresponding maximums. Noting that near the wall  $\omega_y$  is dominated by the streamwise velocity streaks (i.e.  $\omega_y \approx \partial_z u$ ), whose spanwise separation distance is approximately 100 wall units for all  $Re_\tau$  (Jiménez 2012), the profiles of  $\omega_{y,rms}^+$ , thus, are notably  $Re$ -invariant in viscous scalings (figure 6b). On the other hand, the outer flow large-scale structures are more developed along the streamwise and spanwise directions than along the wall-normal direction (due to the constraint by the outer flow boundary), their footprint effects thus result in notable  $Re$ -dependence on  $\omega_{x,rms}^+$  and  $\omega_{z,rms}^+$ .

Figures 7(a) and 7(b) show the  $Re_\tau$  scaling of vorticities variances at the wall. Again, both  $\omega_{z,w}^{2+}$  (also the spanwise wall dissipation rate) and  $\omega_{x,w}^{2+}$  (also the streamwise wall dissipation rate) are in good agreement with the defect power law (3.1). In contrast, previously published logarithmic scalings (Diaz-Daniel *et al.* 2017; Tardu 2017) show notable deviations from the DNS data, particularly for  $\omega_{x,w}^{2+}$ . Note that the data at  $Re_\tau = 10^4$  for  $\omega_{x,w}^{2+}$  in (b) deviate from both the logarithmic and defect power law, which may be due to the small domain size used by Hoyas *et al.* (2022). Notable differences in vorticity fluctuations are observed between OCFs and CCFs in a narrow region near the free surface. For the CCFs, the centreline r.m.s. vorticity fluctuations are almost isotropic, and all components decrease with increasing  $Re_\tau$  (figure 5b). For the OCFs, due to impermeability

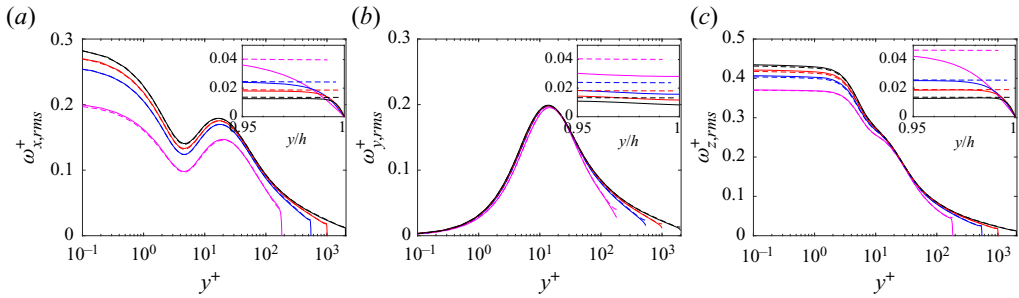


Figure 6. Root-mean-square (r.m.s.) vorticity fluctuations as a function of  $y^+$ : (a)  $\omega_{x,rms}^+$ , (b)  $\omega_{y,rms}^+$  and (c)  $\omega_{z,rms}^+$ . The insets in (a–c) are enlarged views near the free surface.

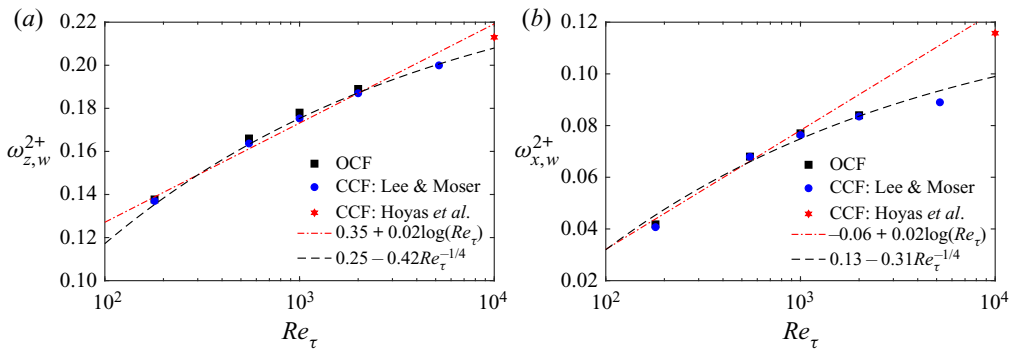


Figure 7. Variations in  $Re_\tau$  of the maximum vorticity fluctuations located at the wall (a)  $\omega_{z,w}^{2+}$  and (b)  $\omega_{x,w}^{2+}$ . The dashed lines indicate logarithmic growth in (3.2), whereas the dash-dotted lines indicate the scaling of Chen & Sreenivasan (2022) in (3.1).

and shear-free boundary condition on the surface, wall-parallel vorticities (i.e.  $\omega_x$  and  $\omega_z$ ) vanish, leading to only non-zero perpendicular vortices attached to the free surface (Pan & Banerjee 1995). As the r.m.s. velocity fluctuations (e.g.  $u_{rms}^+$  or  $w_{rms}^+$ ) on the free surface increase but the wall-normal r.m.s. vorticity fluctuation  $\omega_{y,rms}^+$  decreases, the characteristic eddy length scale, the ratio of the two, increases in wall units with increasing  $Re_\tau$ . In fact, the thickness of the anisotropic vorticity layer where the surface parallel vorticity fluctuation components rapidly drop in OCF is very thin, only approximately 20 wall units according to our data, similar to that observed by Calmet & Magnaudet (2003) based on the large eddy simulation of OCF at  $Re_\tau = 1280$ .

### 3.2. Energy spectra

#### 3.2.1. Premultiplied spectra of streamwise velocity

The separation of scales between the near-wall and outer-layer structures enlarges as  $Re_\tau$  increases. Following previous works (Kim & Adrian 1999; Guala, Hommema & Adrian 2006; Lee & Moser 2015; Duan *et al.* 2020), the one-dimensional velocity spectra are employed here to examine the distribution of energy/Reynolds shear stress at different scales. Figure 8 shows the premultiplied spectrum of the streamwise velocity fluctuations  $k_x \Phi_{uu} / u_\tau^2$  of OCFs for different Reynolds numbers as functions of  $\lambda_x^+$  and  $y^+$ . Consistent with prior findings for other types of wall turbulence (Morrison *et al.* 2002; Schlatter *et al.*

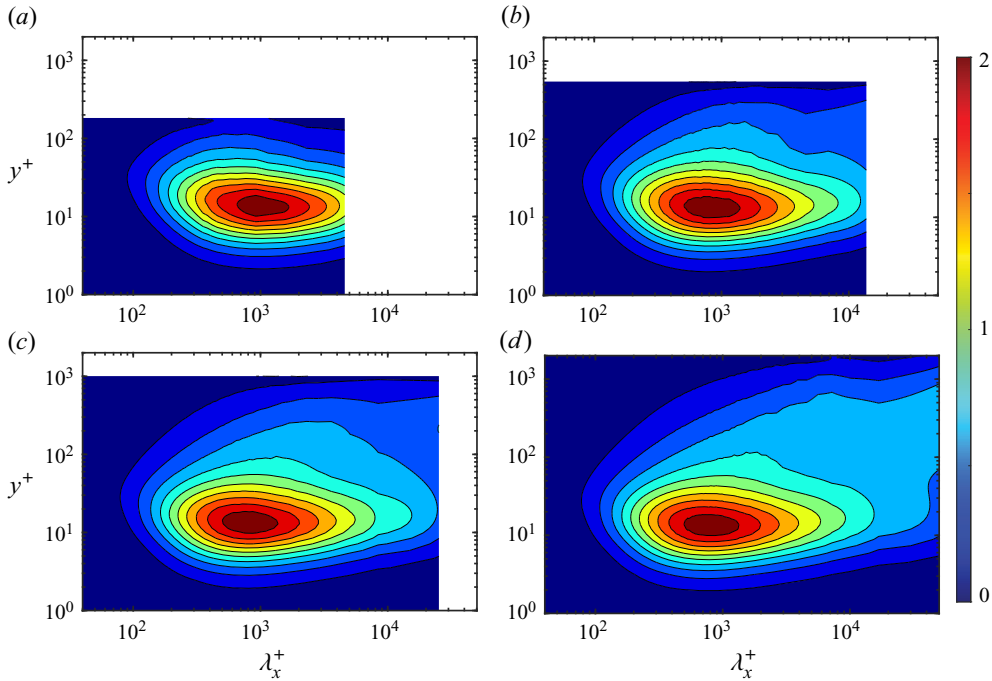


Figure 8. Premultiplied spectra of streamwise velocity  $k_x \Phi_{uu} / u_\tau^2$  as a function of  $\lambda_x^+$  and  $y^+$  for: (a)  $Re_\tau = 180$ , (b)  $Re_\tau = 550$ , (c)  $Re_\tau = 1000$  and (d)  $Re_\tau = 2000$ .

2010; Lee & Moser 2015),  $k_x \Phi_{uu} / u_\tau^2$  exhibits a strong inner peak at  $y^+ \approx 13$  with a typical wavelength  $\lambda_x^+ \approx 1000$ , associated with the energetic near-wall streaks in the buffer layer (Waleffe 1997; Schoppa & Hussain 2002). As  $Re_\tau$  increases, the energy content in the outer region continuously increases. Recent experiments in OCFs (Cameron *et al.* 2017; Wang & Richter 2019; Peruzzi *et al.* 2020) showed that there exist dual peaks in the outer region for  $Re_\tau \geq 550$ , and Duan *et al.* (2020) further found that because of sufficient inner- and outer-scale separation, a distinct outer peak develops for  $Re_\tau \geq 1800$ . The typical wavelengths of these two peaks are around  $O(3h)$  and  $O(20h)$ , which correspond to the scale of LSMs and VLSMs, respectively. These scales are identical to those observed for CCFs and pipe flows (Balakumar & Adrian 2007; Monty *et al.* 2009), but much higher  $Re_\tau$  is required in these flows. As the domain size employed here is comparable to the scale of VLSMs, such dual peaks are not observed in figure 8. Note that in the current numerical set-up, all structures with wavelength  $\lambda_x/h \geq 8\pi$  are considered as streamwise uniform (i.e.  $k_x = 0$ ). As demonstrated in the Appendix, a second peak with streamwise wavelength  $\lambda_x/h$  around 10–20 indeed occurs when the streamwise domain size is doubled (i.e.  $L_x/h = 16\pi$ ).

Figure 9 further shows the premultiplied spanwise spectra of the streamwise velocity fluctuations  $k_z \Phi_{uu} / u_\tau^2$  for different Reynolds numbers. Again, there exists a strong inner peak in the buffer layer  $y^+ \approx 13$  with a typical wavelength  $\lambda_z^+ \approx 100$ , which corresponds to the spanwise spacing of the near-wall streaks. The energy contents at large wavelengths manifest as  $Re_\tau$  increases. For the OCF2000 case, a distinct outer peak occurs with  $\lambda_z \sim 1h$ , which is similar to that identified in CCFs (Jiménez 2012; Lee & Moser 2015). Note that to the best of our knowledge, this is the first time such an outer peak of  $k_z \Phi_{uu}(k_z)$  has been observed for the OCFs.

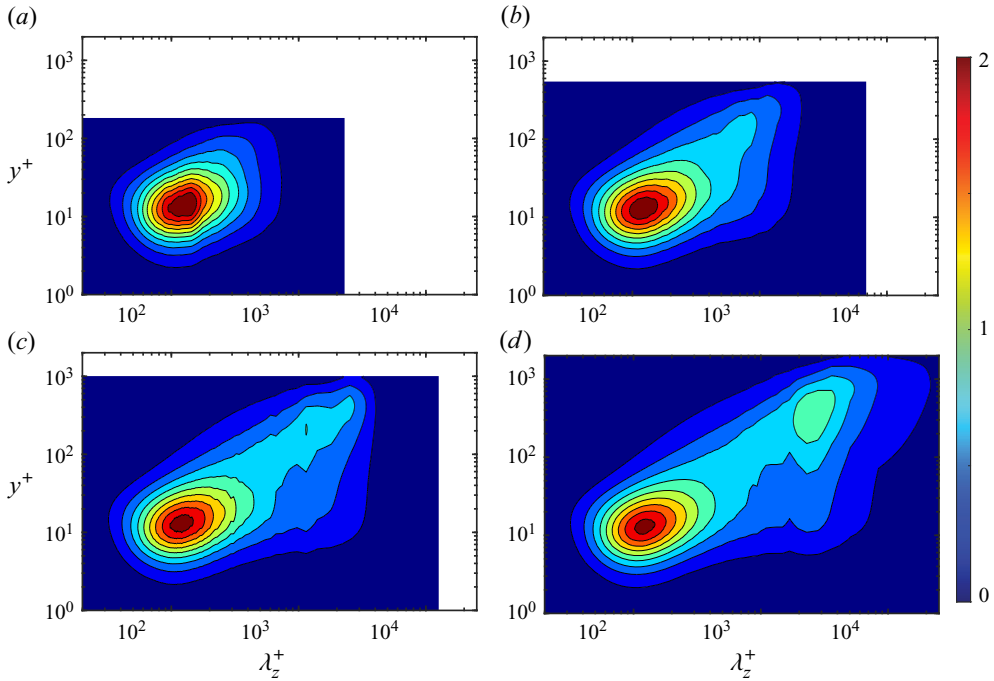


Figure 9. Premultiplied spectra of streamwise velocity  $k_z \Phi_{uu} / u_\tau^2$  as a function of  $\lambda_z^+$  and  $y^+$  for: (a)  $Re_\tau = 180$ , (b)  $Re_\tau = 550$ , (c)  $Re_\tau = 1000$  and (d)  $Re_\tau = 2000$ .

Figure 10 compares the one-dimensional pre-multiplied spectra  $k_x \Phi_{uu}(k_x)$  and  $k_z \Phi_{uu}(k_z)$  at different  $y$  locations between OCF and CCFs for  $Re_\tau = 2000$ . Note that the area under the curves is proportional to the scaled turbulence intensity of the streamwise velocity. A good agreement between OCF and CCF is observed at  $y^+ = 15$ , particularly at small wavenumbers, suggesting that the near-wall coherent structures in OCFs have similar characteristics as other wall turbulence. In the overlap and outer region, both  $k_x \Phi_{uu}$  and  $k_z \Phi_{uu}$  are slightly smaller in OCFs than in CCFs at small wavenumbers, but the trend reverses at large wavenumbers. It indicates that the large-scale structures are more energetic in OCFs than CCFs. This can be further confirmed by examining the cumulative contributions to Reynolds stresses from all wavenumbers between 0 and  $k = 2\pi/\lambda^c$ , which is defined as (Balakumar & Adrian 2007; Duan *et al.* 2020)

$$\gamma_{ij}(k^c) = \frac{\int_0^k \Phi_{ij}(\tilde{k}) d\tilde{k}}{\int_0^\infty \Phi_{ij}(\tilde{k}) d\tilde{k}}. \quad (3.3)$$

In the literature (e.g. Bernardini & Pirozzoli 2011; Dogan *et al.* 2019),  $\lambda_x = 3h$  or  $\lambda_z = h$  is widely used to separate LSMs and VLSMs. Figure 11 shows the fraction of kinetic energy carried by VLSMs as a function of  $y/h$  for  $Re = 550, 1000$  and  $2000$  cases. The results from the CCFs are also included for comparison. Consistent with the finding in Duan *et al.* (2020),  $\gamma_{uu}(\lambda_x = 3h)$  is 0.5–0.65 in the outer region of OCFs (e.g.  $y/h > 0.2$ ). The contribution of VLSMs to the streamwise kinetic energy is even higher when calculated based on the spanwise wavelength (i.e.  $\lambda_z = 0.5h$ ). It suggests that VLSMs contribute most to the streamwise Reynolds stress in the outer region. In addition, at the same  $Re_\tau$ , the streamwise kinetic energy carried by VLSMs is notably larger in OCFs than in CCFs, confirming that VLSMs are stronger in the former.

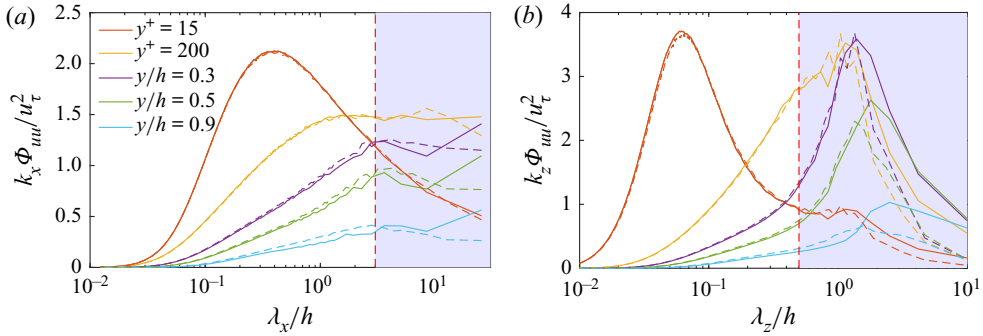


Figure 10. Comparison of premultiplied spectra of streamwise velocity (a)  $k_x \Phi_{uuu}$  and (b)  $k_z \Phi_{uuu}$  at different  $y$  locations for  $Re_\tau = 2000$ . The solid and dashed lines represent OCF and CCF, respectively.

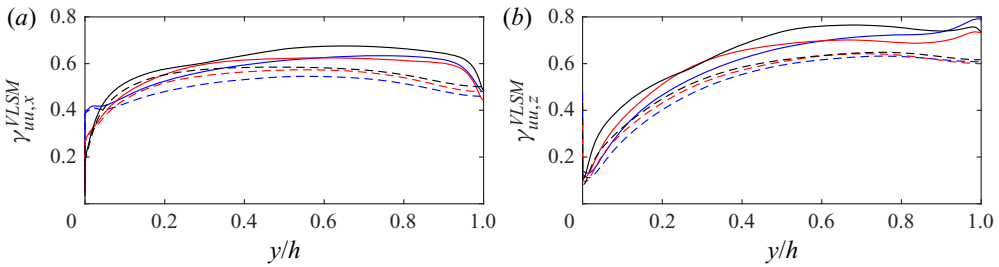


Figure 11. The fraction of kinetic energy carried by VLSMs defined based on (a)  $\lambda_x > 3h$  and (b)  $\lambda_z > 0.5h$ . The legend for line types and symbols is also given tables 1 and 2.

Further insights into the distribution of scales can be gained from figure 12, where we show instantaneous streamwise velocity fluctuations  $u'$  in wall-parallel ( $x$ - $z$ ) planes at different wall-normal locations for  $Re_\tau = 2000$ . The  $u'$  close to the wall exhibits the organisation of the streaks with a streamwise length of approximately 1000 and spanwise spacing of 100. Consistent with the previous findings (Hutchins & Marusic 2007; Bernardini *et al.* 2014), the outer layer flow exhibits very long regions of positive/negative  $u'$ . Similar to the finding from energy spectra (figure 9), these streamwise meandering streaks have characteristic lengths  $\lambda_z \approx h$  in the spanwise directions. These streaks can be interpreted in terms of large-scale structures that in the form of streamwise vortices of diameters comparable to the channel height (Tamburrino & Gulliver 1999; Duan *et al.* 2020) or spatial clusters of hairpin vortices (Kim & Adrian 1999). In addition, these structures have their footprint both near the wall and the free surface.

Compared with the CCFs (Bernardini *et al.* 2014), more small scales are observed at  $y/h = 1$  in OCFs (figure 12d). This can be further confirmed by showing the instantaneous wall-normal vorticity  $\omega_y$  on the free surface for  $Re_\tau = 2000$  (figure 13a). Numerous small-scale  $\omega_y$  patches (with both positive and negative signs) are observed. Figures 13(b) and 13(c) further show the vortical structures (visualised using the  $\lambda_2$  criterion) near the free surface in regions I and II of figure 13(a). Compared with CCFs, more small-scale  $\lambda_2$  structures are observed, mainly due to a stronger boundary layer effect near the free surface (Wang *et al.* 2017). As expected, among these structures, some are aligned along the wall-normal direction, which might be generated due to the Kelvin–Helmholtz instability of the free-surface vortex sheet. There also exists significant amounts of  $\lambda_2$  vortices that are parallel to the wall. Furthermore, different from the near-wall vortices,

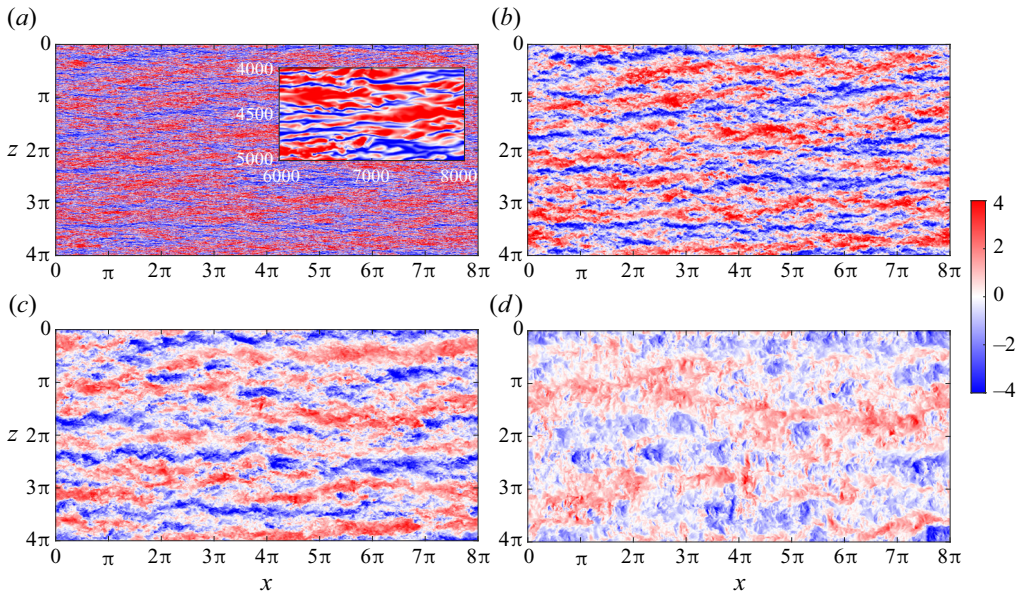


Figure 12. Instantaneous streamwise velocity fluctuations ( $u'/u_\tau$ ) for  $Re_\tau = 2000$  in  $x$ - $z$  planes at (a)  $y^+ = 15$ , (b)  $y^+ = 384$  ( $y/h = 0.19$ ), (c)  $y/h = 0.5$  and (d)  $y/h = 1$ . The inset in (a) shows an enlarged view of a box with  $2000 \times 1000$  in wall units.

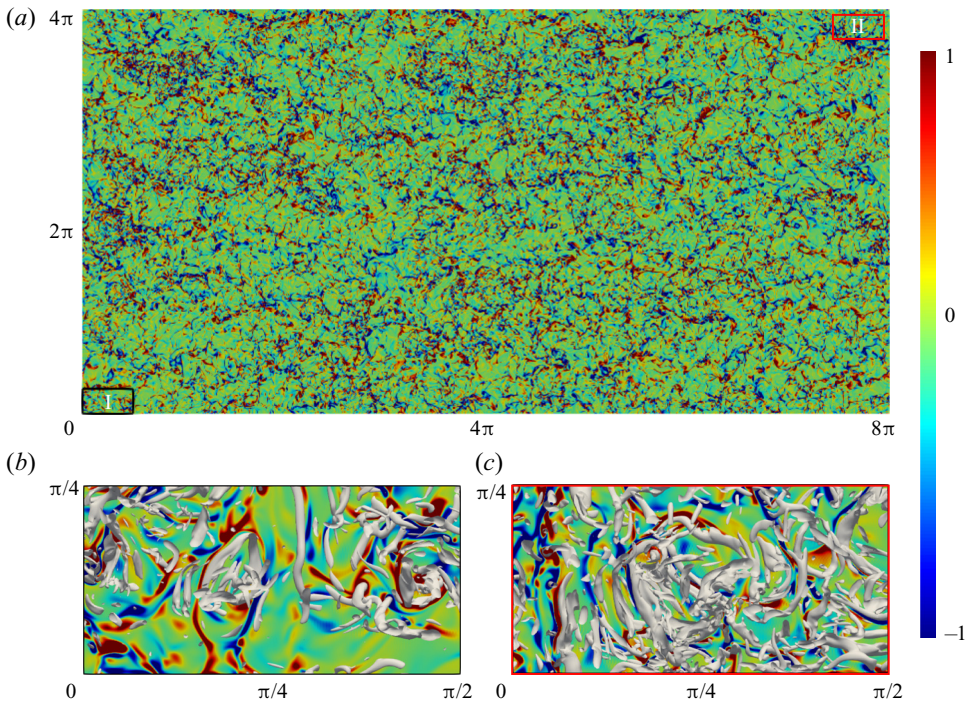


Figure 13. (a) Instantaneous wall-normal vorticity  $\omega_y$  (normalised by its r.m.s. value) on the free surface for  $Re_\tau = 2000$  and enlarged view of (b) box I and (c) box II along with the vortical structures visualised using the  $\lambda_2$  criterion within  $\Delta y^+ \leq 200$  from the free surface.

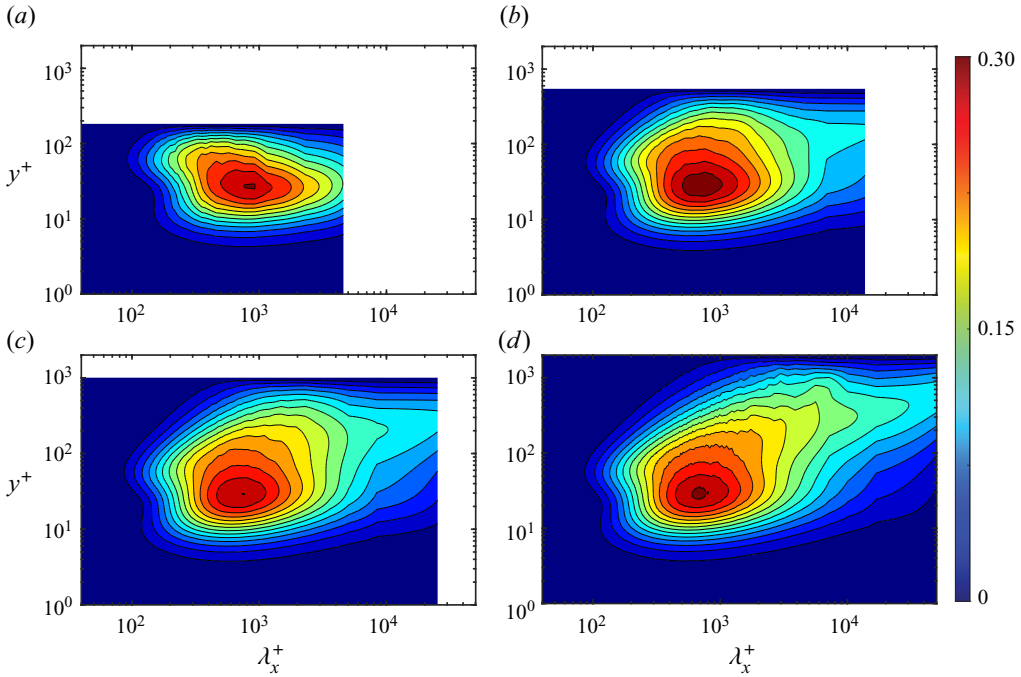


Figure 14. Premultiplied cospectra of streamwise and wall-normal velocities  $k_x \Phi_{uv} / u_\tau^2$  as a function of  $\lambda_x^+$  and  $y^+$  for: (a)  $Re_\tau = 180$ , (b)  $Re_\tau = 550$ , (c)  $Re_\tau = 1000$  and (d)  $Re_\tau = 2000$ .

which are predominantly aligned along the streamwise direction, the wall-parallel vortices near the free surface have relatively larger tilting angle with respect to the streamwise direction. Interestingly, some of these vortices are even oriented along the spanwise direction, which is consistent with the recent finding by Duan *et al.* (2021a) that higher relative population density of spanwise vortices occurs in OCFs than in CCFs. Based on the ‘bottom-up’ perspective for the origin of VLSMs, in which VLSMs are viewed as the result of coherence in the pattern of vortices produced near the boundary (Kim & Adrian 1999), these additional vortical structures near the free surface may be one possible explanation for the increased VLSMs in OCFs: a topic that merits further study.

### 3.2.2. Premultiplied spectra of Reynolds shear stress

To investigate the contribution of VLSMs to the Reynolds shear stress and also to the mean wall shear stress, premultiplied cospectra of streamwise and wall-normal velocities are examined here. Figures 14 and 15, respectively, show the premultiplied cospectra  $k_x \Phi_{uv} / u_\tau^2$  and  $k_z \Phi_{uv} / u_\tau^2$  for different Reynolds numbers in wall units. Similar to the streamwise velocity spectra  $k \Phi_{uu}$  (figures 8 and 9), an inner peak is observed, which is associated with the near-wall coherent structures. The peak occurs at a higher  $y^+$  when compared with  $k \Phi_{uu}$ . As  $Re_\tau$  increases, the energy content in the outer region continues to increase, and a second peak located at  $\lambda_z = h$  starts to occur at  $Re_\tau = 2000$  for the  $k_z \Phi_{uv} / u_\tau^2$  (similar to  $k_z \Phi_{uu} / u_\tau^2$  in figure 10e), but not for  $k_x \Phi_{uv} / u_\tau^2$  (again due to limited streamwise domain size).

Figure 16 compares the one-dimensional premultiplied cospectra of streamwise and wall-normal velocities  $k_x \Phi_{uv}$  and  $k_z \Phi_{uu}$  at different  $y$  locations for  $Re_\tau = 2000$ . Again,

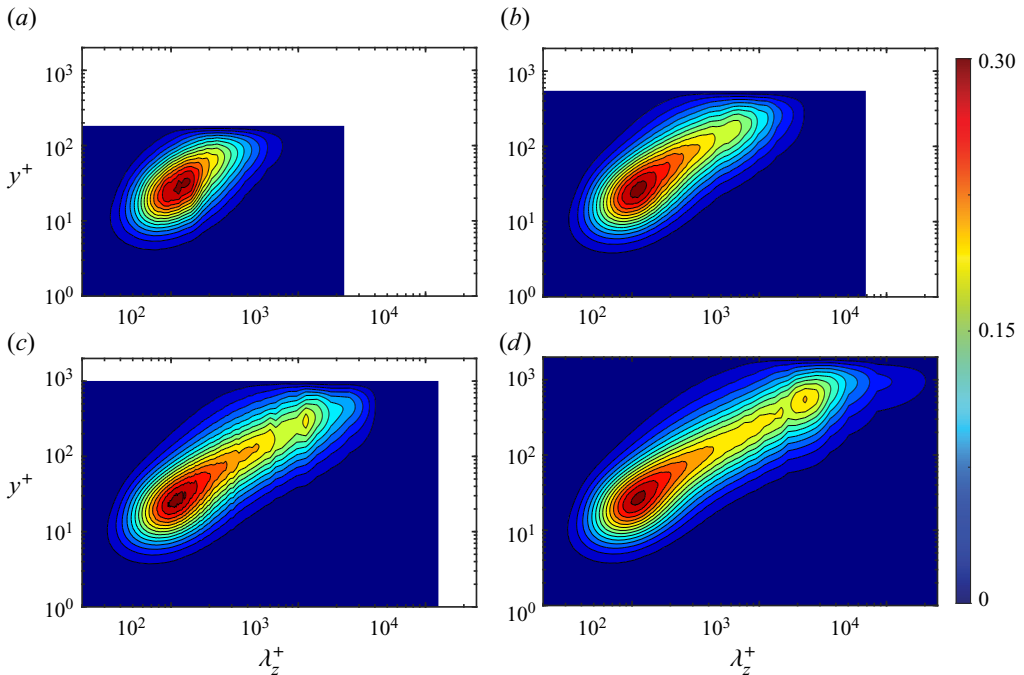


Figure 15. Premultiplied cospectra of streamwise and wall-normal velocities  $k_z \Phi_{uv} / u_\tau^2$  as a function of  $\lambda_z^+$  and  $y^+$  for: (a)  $Re_\tau = 180$ , (b)  $Re_\tau = 550$ , (c)  $Re_\tau = 1000$  and (d)  $Re_\tau = 2000$ .

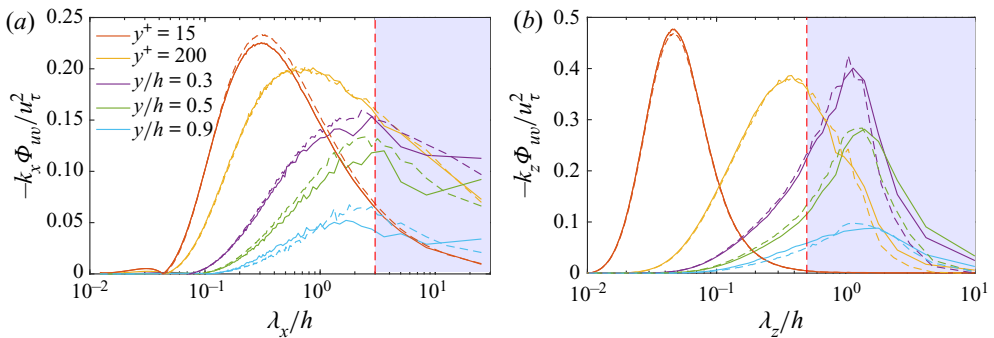


Figure 16. Premultiplied cospectra of streamwise and wall-normal velocities (a)  $k_x \Phi_{uv}$  and (b)  $k_z \Phi_{uv}$  at different  $y$  locations for  $Re_\tau = 2000$ . The solid and dashed lines represent OCF and CCF, respectively.

good collapse can be observed between OCF and CCF in the near-wall region (e.g. at  $y^+ = 15$ ). In the overlap region, both  $k_x \Phi_{uv}$  and  $k_z \Phi_{uv}$  are slightly smaller in OCF than in CCF at small wavelengths, but the trend reverses at large wavelengths, akin to those observed for the streamwise velocity spectra. Interestingly, very close to the free surface (e.g. at  $y/h = 0.9$ ), both  $k_x \Phi_{uv}$  and  $k_z \Phi_{uv}$  become larger again in OCFs at small  $\lambda_x$  and  $\lambda_z$ , confirming the prominence of small-scale structures due to the boundary layer effect of the free surface (figure 13). This is also consistent with the finding by Wang *et al.* (2017), who showed that the free surface restrains the characteristic scales of the streaks and the associated vortical structures. Following (3.3), figures 17(a) and 17(b) show the fraction of Reynolds shear stress carried by VLSMs:  $\gamma_{uv}(\lambda_x = 3h)$  and  $\gamma_{uv}(\lambda_z = 0.5h)$ . Both of them increase with  $y$  and reach approximately 0.5–0.6 at  $y/h = 0.5$  and then decrease near the



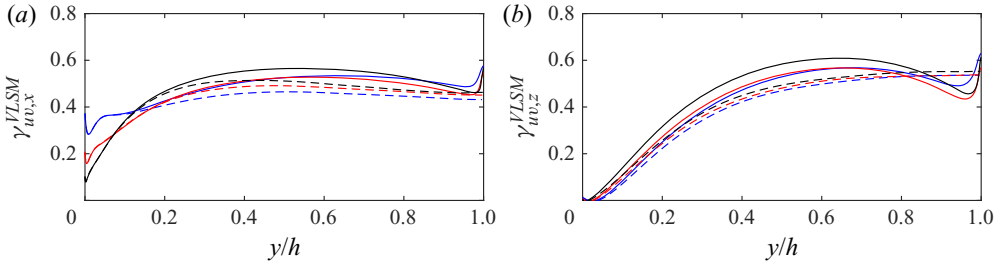


Figure 17. The fraction of Reynolds shear stress carried by VLSMs defined based on (a)  $\lambda_x > 3h$  and (b)  $\lambda_z > 0.5h$ . The legend of line types and symbols is also given tables 1 and 2.

Case	$Re_\tau$	$Re_b$	$10^3 C_f$	$C_f^L$	$C_f^T$	$C^L/C_f(\%)$	$C^T/C_f(\%)$
OCF180	182	2857	8.17	2.10	6.07	25.7	74.3
OCF550	547	10 000	5.98	0.60	5.38	10.0	90.0
OCF1000	1004	20 000	4.98	0.30	4.68	6.0	94.0
OCF2000	2006	43 478	4.27	0.13	4.14	3.0	97.0
CCF180	182	2857	8.13	2.10	6.03	25.8	74.2
CCF550	544	10 000	5.92	0.60	5.32	10.0	90.0
CCF1000	998	20 000	4.98	0.30	4.68	6.0	94.0
CCF2000	1996	43 478	4.22	0.13	4.09	3.1	96.9

Table 3. The skin friction coefficient and its decomposition based on FIK identity.

free surface, particularly for the spanwise case. Again, at a given  $Re_\tau$ , the maximum values are slightly larger than that for CCF, highlighting the free surface effect in OCFs.

### 3.3. Scale contribution to the skin friction

In this section, we further investigate the contributions of different scale motions to the mean wall shear stress (or, equivalently, the skin friction) and compare the difference between OCFs and CCFs. Based on the Fukagata–Iwamoto–Kasagi (FIK) identity (Fukagata, Iwamoto & Kasagi 2002), the skin friction coefficient can be directly linked to the alteration of the Reynolds shear stress:

$$C_f = \underbrace{\frac{6}{Re_b}}_{C_f^L} + \underbrace{\frac{6}{U_b^2} \int_0^1 (1-y)(-\langle u'v' \rangle) dy}_{C_f^T}, \quad (3.4)$$

which has been obtained for OCF by Duan *et al.* (2021b). The skin friction coefficient  $C_f \equiv 2\tau_w/(\rho U_b^2)$  thus has an ‘equivalent’ laminar part  $C_f^L$ , and a turbulent part  $C_f^T$  represented by the weighted integration of the total Reynolds shear stress. Table 3 lists the estimated skin friction using (3.4) at different Reynolds numbers. Note that for all cases, the relative error of  $C_f$  between the direct calculation based on the definition and the FIK identity is within  $\pm 1\%$ . In addition, at the same Reynolds number,  $C_f$  and its laminar and turbulent components are identical between OCFs and CCFs. As expected, the turbulent contribution becomes larger as  $Re_\tau$  increases, changing from approximately 74% at  $Re_\tau = 200$  to 97% at  $Re_\tau = 2000$ .

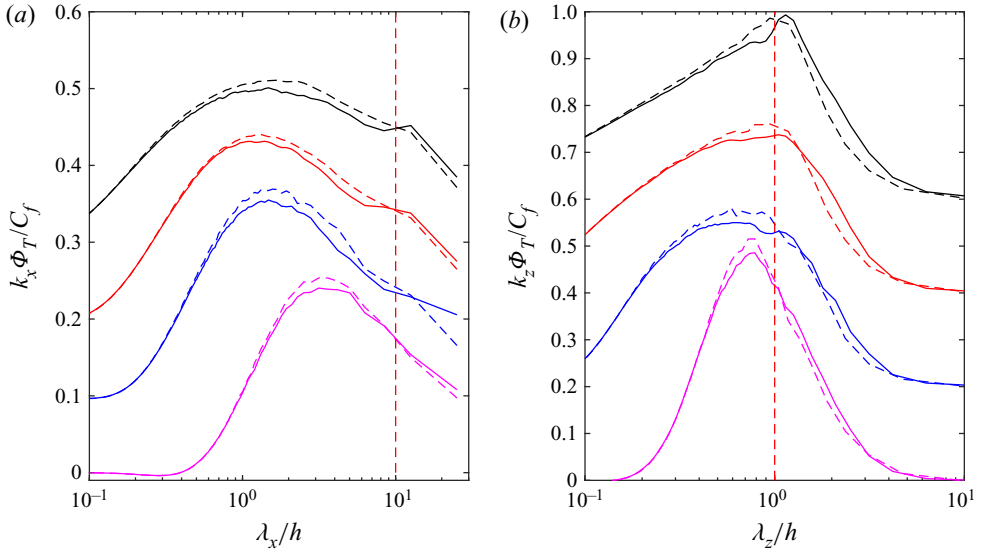


Figure 18. Comparison of (a)  $k_x \Phi_T / C_f$  and (b)  $k_z \Phi_T / C_f$  between OCF (solid) and CCF (dashed) cases. For better display, the curves are vertically shift by 0.1 and 0.2 in (a,b), respectively.

To further quantify the contributions to  $C_f$  from different scales, the FIK identity in combination with the wavenumber spectra of the Reynolds shear stress (Deck *et al.* 2014; Yao, Chen & Hussain 2019) is employed. The total Reynolds shear stress can be expressed in terms of one-dimensional Reynolds shear stress spectral density, i.e.

$$-\langle u'v' \rangle (y) = \int_{-\infty}^{\infty} \Phi_{uv}(y; k) dk. \tag{3.5}$$

Therefore, (3.4) can be further expressed as

$$C_f = \frac{6}{Re_b} + \frac{6}{U_b^2} \int_0^1 \int_{-\infty}^{\infty} (1-y) \Phi_{uv}(y; k) dk dy, \tag{3.6}$$

$$= \frac{6}{Re_b} + \underbrace{\int_{-\infty}^{\infty} \int_0^1 \frac{6}{U_b^2} (1-y) \Phi_{uv}(y; k) dy}_{\Phi_T} dk. \tag{3.7}$$

Then, the contribution of a specific length scale to  $C_f$  can be represented by  $\Phi_T(k)$ .

Figure 18(a,b) shows the  $k_x \Phi_T / C_f$  and  $k_z \Phi_T / C_f$  as a function of  $\lambda_x$  and  $\lambda_z$ , respectively. Note that the total area below curve  $k_x \Phi_T / C_f$  and  $k_z \Phi_T / C_f$  equals the total ‘turbulent’ contribution to  $C_f$ . Except for the OCF180 case,  $k_x \Phi_T / C_f$  peaks at  $\lambda_x = 1 \sim 2h$ , consistent with the observation by Duan *et al.* (2021b). In addition, for the OCF2000 case, a second peak develops around  $\lambda_x = 10h$ , which corresponds to the contribution from VLSMs. For  $k_z \Phi_T / C_f$ , the location of the peak shifts towards larger  $\lambda_z$  with increasing  $Re_\tau$  and becomes  $\lambda_z = 1h$  for  $Re_\tau = 2000$ , which is due to the dominant role of VLSMs to the Reynolds shear stress at high  $Re_\tau$ . Although the shape is similar between OCF and CCF, notable differences can be observed. In the wavelength range of  $\lambda_x < 10h$  (or  $\lambda_z < h$ ), the  $k_x \Phi_T / C_f$  ( $k_z \Phi_T / C_f$ ) in OCF is smaller than that in CCF. However, the trend reverses for  $\lambda_x > 10h$  ( $\lambda_z > 1h$ ), suggesting a high contribution to  $C_f$  for turbulent motions at very large length scales in OCFs.

DNS of open channel flows

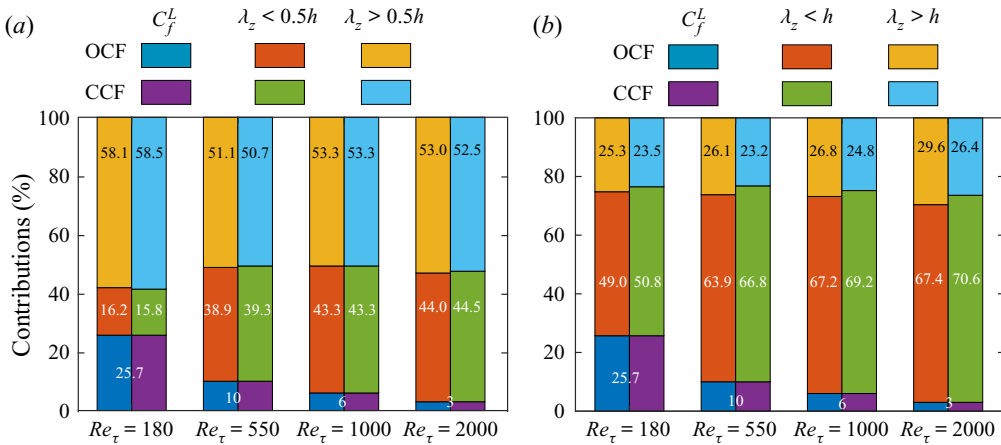


Figure 19. Contributions of different scales to the skin friction by using the cut-off wavelength (a)  $\lambda_z = 0.5h$  and (b)  $\lambda_z = 1h$ .

Due to limited streamwise domain size,  $k_x \Phi_T / C_f$  still remains relatively large at the largest  $\lambda_x$  considered, whereas  $k_z \Phi_T / C_f$  decays to zero at large  $\lambda_z$ , suggesting the adequacy of the spanwise domain size. In the following, we further employ  $k_z \Phi_T / C_f$  to determine the contribution to skin friction from a range of scales. The cumulative turbulent contribution is defined as

$$Cum_T(\lambda_z) = \int_{2\pi/\lambda_z}^{\infty} k_z \Phi_T / C_f dk_z, \quad (3.8)$$

which represents the total turbulent contributions for all spanwise scales smaller than a given wavelength  $\lambda_z$ . By choosing appropriate cut-off wavelength ranges, the contribution from the specified scale range can be obtained. For example, figure 19(a) shows the fractions contributed by different scales when choosing the typical cut-off wavelength  $\lambda_z = 0.5h$  to separate LSMs and VLSMs. With this threshold, there is a negligible difference between OCFs and CCFs. Although the laminar contribution to  $C_f$  decreases with increasing  $Re_\tau$ , the contribution from turbulent motions with wavelength  $\lambda_z < 0.5h$  increases continuously, becoming approximately 44% at  $Re_\tau = 2000$ . In addition, for all cases, the VLSMs (with a spanwise wavelength  $\lambda_z > 0.5h$ ) contribute more than 50%. Further results are obtained by using a larger dividing wavelength of  $\lambda_z = 1h$  (figure 19b). The contribution to  $C_f$  from turbulent motions with  $\lambda_z > 1h$  continuously increases with  $Re_\tau$ . It becomes approximately 30% at  $Re_\tau = 2000$  in OCFs, slightly higher than that in CCFs, which is consistent with the observation in figure 18. Most importantly, the discrepancy between OCFs and CCFs seems to enlarge with  $Re_\tau$ , suggesting that at very high Reynolds numbers, the contribution from VLSMs to the Reynolds shear stress and also to skin friction would be quite different.

Note that the above analysis based on the FIK analysis and spectra decomposition have certain caveats. For example, there is a lack of physical interpretation for the linear weight of Reynolds shear stress in (3.4). To overcome this issue, many other skin friction decomposition methods have been proposed (e.g. Renard & Deck 2016; Chen, Yao & Hussain 2021). In addition, we assume that the turbulent motions of a particular scale can be fully represented by a specific Fourier mode. This might not reflect the true flow physics in wall turbulence considering the modulation effects may spread over a wide range of Fourier modes (Ganapathisubramani *et al.* 2012).

#### 4. Conclusions

DNS of turbulent OCF for friction Reynolds number  $Re_\tau$  up to 2000 have been presented. Various flow statistics are collected and compared with the CCFs. As expected, the mean velocity profiles between OCFs and CCFs collapse in the near-wall region but differ in the outer region. In particular, due to the presence of the free surface, the wake region is smaller in OCFs. In addition, different from CCFs, a distinct log layer with Kármán constant  $\kappa = 0.363$  is observed for OCF at  $Re_\tau = 2000$ , whereas the range is further away from the wall (i.e.  $y/h$  from 0.25 to 0.6) compared with the usual log layer. Except for a very thin layer near the free surface, the Reynolds stresses and vorticity fluctuations agree well between OCFs and CCFs. The Reynolds number scaling of the near-wall averaged quantities, particularly the vorticity variances at the wall, seem to follow closely the defect power law proposed by Chen & Sreenivasan (2021, 2022).

Contributions of different scales to the turbulence statistics are quantified based on the energy spectra. The very-large-scale structures (with streamwise wavelength  $\lambda_x > 3h$  or spanwise wavelength  $\lambda_z > 0.5h$ ) are shown to make a significant contribution to turbulence statistics, with over 60% of streamwise turbulence intensity and Reynolds shear stress in the overlap and outer layers. In addition, these structures maintain higher strength in the outer layer when compared with the CCFs, suggesting that the free surface can sustain/promote VLSMs. The higher strength of VLSMs is also the main reason for the higher streamwise turbulence intensity in the outer region. Flow visualisations reveal that more small-scale structures are generated near the free surface, presumably due to its boundary layer effect. According to the ‘bottom-up’ perspective of the VLSMs’ origin, these structures might be one of the main reasons for the enhanced VLSMs in OCFs. Further studies are still required to better explain how the free surface affects the VLSMs. Finally, the contribution to the mean wall shear stress from scales with  $\lambda_z > h$  increases with Reynolds number and becomes approximately 30% at  $Re_\tau = 2000$ , slightly higher than the CCFs at the same  $Re_\tau$ . As a conclusion, the presence of the free surface in OCFs has significant effects on flow dynamics, such as the development of the log layer in the mean velocity profile at lower  $Re_\tau$ , redistribution of turbulent kinetic energy and the enhancement of VLSMs.

**Acknowledgements.** We appreciate M. Lee and R. Moser for providing us with their channel flow code, which is used for this study. We are also grateful to Q. Zhong for providing the experimental data. Computational resources provided by Texas Tech University HPCC, TACC Lonestar, Stampede2 and Frontera are acknowledged.

**Funding.** J.Y. and F.H. are funded by TTU Distinguished Chair. X.C. acknowledges support from the National Natural Science Foundation of China, grant numbers 12072012, 11721202 and 91952302, and “the Fundamental Research Funds for the Central Universities”.

**Declaration of interests.** The authors report no conflict of interest.

**Data availability statement.** The data that support the findings of this study are openly available in Texas Data Repository at <https://dataverse.tdl.org/dataverse/toclf/>.

**Author ORCIDs.**

 Jie Yao <https://orcid.org/0000-0001-6069-6570>;

 Xi Chen <https://orcid.org/0000-0002-4702-8735>;

 Fazle Hussain <https://orcid.org/0000-0002-2209-9270>.

Case	$L_x/h, L_z/h$	$N_x \times N_z$	$Tu_\tau/h$
OCF550S	$4\pi, 2\pi$	$768 \times 768$	47
OCF550M1	$4\pi, 4\pi$	$768 \times 1536$	10.4
OCF550M2	$8\pi, 2\pi$	$1536 \times 768$	12.6
OCF550SL	$16\pi, 4\pi$	$3072 \times 1536$	10.1
OCF2000SL	$16\pi, 2\pi$	$8192 \times 2048$	3.3

Table 4. Details of the numerical discretisation employed for the OCF simulations. The computational box size is  $L_x \times L_y \times L_z$ , with  $h$  the channel height; and  $N_x, N_y$  and  $N_z$  are the number of grid sizes in each direction. Here  $Tu_\tau/h$  is the total simulation time without transition.

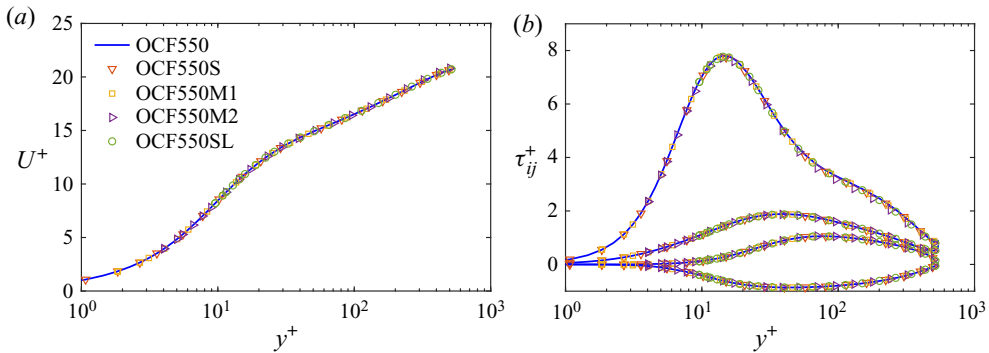


Figure 20. (a) Mean velocity and (b) Reynolds stress as a function of  $y^+$  for different domain size effect at  $Re_\tau = 550$ .

### Appendix. Domain size effect in turbulent OCFs

The effect of domain size on flow statistics and structures is further examined here. We first perform additional DNS with various streamwise and spanwise lengths at  $Re_\tau = 550$ . The details of domain sizes, grid sizes and resolutions are listed in table 4. Figure 20 shows the mean streamwise velocity and Reynolds stress profiles for different domain size cases. The agreement between them is reasonably good across the whole channel, consistent with the findings by Lozano-Durán & Jiménez (2014) for the CCFs. Figures 21(a) and 21(b) further shows the premultiplied streamwise and spanwise spectra of the streamwise velocity fluctuations  $k_x \Phi_{uu}/u_\tau^2$  and  $k_z \Phi_{uu}/u_\tau^2$  for different domain size cases. The spectrum of  $k_x \Phi_{uu}/u_\tau^2$  is truncated by the box, particularly for the shorter streamwise domain size cases. However, for all cases, the contours collapse at small wavelengths and differ at large ones. Even for this large streamwise domain, the lowest contour ( $k_x \Phi_{uu}/u_\tau^2 = 0.2$ ) is not closed. For the largest streamwise domain size case (i.e. OCF550SL), a second peak located at  $\lambda_x^+ = 10\,000$  (or  $\lambda_x/h \approx 18$ ) develops in the outer region. The  $k_z \Phi_{uu}/u_\tau^2$  spectrum is closed for all cases, indicating  $L_z = 2\pi$  is wide enough to capture most energy of the streamwise velocity fluctuations. Although the contours collapse at small  $\lambda_z^+$ , they differ at larger  $\lambda_z^+$ , particularly near the free surface. This suggests that the spanwise domain size has a notable effect on the distributions of energy and Reynolds stress, particularly at large scales.

Finally, an additional case (i.e. OCF2000SL) with double the streamwise domain size but half the spanwise domain size as OCF2000 is considered. Figure 22 compares the premultiplied streamwise and spanwise spectra of the streamwise velocity fluctuations

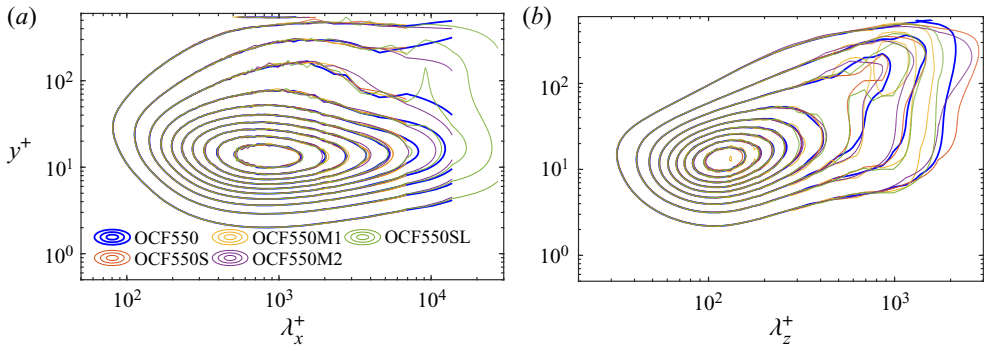


Figure 21. Premultiplied streamwise and spanwise spectra of the streamwise velocity fluctuations (a)  $k_x \Phi_{uu}/u_\tau^2$  and (b)  $k_z \Phi_{uu}/u_\tau^2$  for different domain sizes at  $Re_\tau = 550$ .

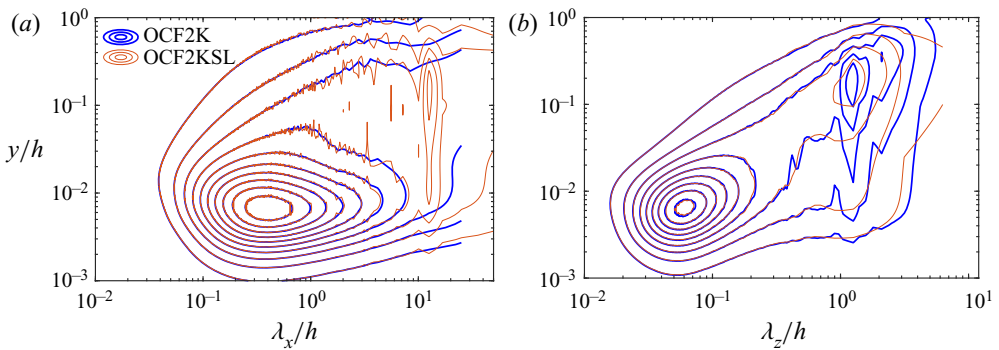


Figure 22. Premultiplied streamwise and spanwise spectra of the streamwise velocity fluctuations (a)  $k_x \Phi_{uu}/u_\tau^2$  and (b)  $k_z \Phi_{uu}/u_\tau^2$  for two different domain size cases at  $Re_\tau = 2000$ .

$k_x \Phi_{uu}/u_\tau^2$  and  $k_z \Phi_{uu}/u_\tau^2$  in outer units. Again, the contours collapse at small wavelengths for both cases. The  $k_x \Phi_{uu}/u_\tau^2$  spectrum is truncated by the box for OCF2000 case. However, for the OCF2000SL case, although the lowest contour ( $k_x \Phi_{uu}/u_\tau^2 = 0.2$ ) is not closed, a distinct outer peak develops with streamwise wavelength  $\lambda_x/h = 4\pi$ , larger than that observed by Lee & Moser (2015) for CCF at  $Re_\tau = 2000$ . The spectrum of  $k_z \Phi_{uu}/u_\tau^2$  has a similar shape as that at  $Re_\tau = 550$ , but the outer peak located at  $\lambda_z/h \approx 2\pi/5$  is much stronger.

#### REFERENCES

- AFZAL, N. & YAJNIK, K. 1973 Analysis of turbulent pipe and channel flows at moderately large Reynolds number. *J. Fluid Mech.* **61** (1), 23–31.
- AGHAEI JOUYBARI, M., BRERETON, G.J. & YUAN, J. 2019 Turbulence structures over realistic and synthetic wall roughness in open channel flow at  $Re_\tau = 1000$ . *J. Turbul.* **20** (11–12), 723–749.
- BALAKUMAR, B.J. & ADRIAN, R.J. 2007 Large- and very-large-scale motions in channel and boundary-layer flows. *Phil. Trans. R. Soc. A* **365** (1852), 665–681.
- BAUER, C. 2015 Direct numerical simulation of turbulent open channel flow. Master’s thesis, Karlsruhe Institute of Technology.
- BERGSTROM, D.J., TACHIE, M.F. & BALACHANDAR, R. 2001 Application of power laws to low Reynolds number boundary layers on smooth and rough surfaces. *Phys. Fluids* **13** (11), 3277–3284.

- BERNARDINI, M. & PIROZZOLI, S. 2011 Inner/outer layer interactions in turbulent boundary layers: a refined measure for the large-scale amplitude modulation mechanism. *Phys. Fluids* **23** (6), 061701.
- BERNARDINI, M., PIROZZOLI, S. & ORLANDI, P. 2014 Velocity statistics in turbulent channel flow up to. *J. Fluid Mech.* **742**, 171–191.
- BONAKDARI, H., LARRARTE, F., LASSABATERE, L. & JOANNIS, C. 2008 Turbulent velocity profile in fully-developed open channel flows. *Environ. Fluid Mech.* **8** (1), 1–17.
- CALMET, I. & MAGNAUDET, J. 2003 Statistical structure of high-Reynolds-number turbulence close to the free surface of an open-channel flow. *J. Fluid Mech.* **474**, 355–378.
- CAMERON, S.M., NIKORA, V.I. & STEWART, M.T. 2017 Very-large-scale motions in rough-bed open-channel flow. *J. Fluid Mech.* **814**, 416–429.
- CHAUDHRY, M.H. 2007 *Open-Channel Flow*. Springer Science & Business Media.
- CHEN, X., HUSSAIN, F. & SHE, Z.S. 2019 Non-universal scaling transition of momentum cascade in wall turbulence. *J. Fluid Mech.* **871**, R2.
- CHEN, X. & SREENIVASAN, K.R. 2021 Reynolds number scaling of the peak turbulence intensity in wall flows. *J. Fluid Mech.* **908**, R3.
- CHEN, X. & SREENIVASAN, K.R. 2022 Law of bounded dissipation and its consequences in turbulent wall flows. *J. Fluid Mech.* **933**, A20.
- CHEN, X., YAO, J. & HUSSAIN, F. 2021 Theoretical framework for energy flux analysis of channels under drag control. *Phys. Rev. Fluids* **6** (1), 013902.
- DECK, S., RENARD, N., LARAUFIE, R. & WEISS, P.-É. 2014 Large-scale contribution to mean wall shear stress in high-Reynolds-number flat-plate boundary layers up to  $Re_\theta = 13\,650$ . *J. Fluid Mech.* **743**, 202–248.
- DIAZ-DANIEL, C., LAIZET, S. & VASSILICOS, J.C. 2017 Wall shear stress fluctuations: mixed scaling and their effects on velocity fluctuations in a turbulent boundary layer. *Phys. Fluids* **29**, 055102.
- DOGAN, E., ÖRLÜ, R., GATTI, D., VINUESA, R. & SCHLATTER, P. 2019 Quantification of amplitude modulation in wall-bounded turbulence. *Fluid Dyn. Res.* **51** (1), 011408.
- DUAN, Y., CHEN, Q., LI, D. & ZHONG, Q. 2020 Contributions of very large-scale motions to turbulence statistics in open channel flows. *J. Fluid Mech.* **892**, A3.
- DUAN, Y., ZHONG, Q., WANG, G., CHEN, Q., WANG, F. & LI, D. 2021a Additional spanwise vortices near the free surface in open channel flows. *J. Fluid Mech.* **924**, R3.
- DUAN, Y., ZHONG, Q., WANG, G., ZHANG, P. & LI, D. 2021b Contributions of different scales of turbulent motions to the mean wall-shear stress in open channel flows at low-to-moderate Reynolds numbers. *J. Fluid Mech.* **918**, A40.
- FINLEY, P.J., PHOE, K.C. & POH, J. 1966 Velocity measurements in a thin turbulent water layer. *La Houille Blanche* **6**, 713–721.
- FUKAGATA, K., IWAMOTO, K. & KASAGI, N. 2002 Contribution of Reynolds stress distribution to the skin friction in wall-bounded flows. *Phys. Fluids* **14** (11), L73–L76.
- GANAPATHISUBRAMANI, B., HUTCHINS, N., MONTY, J.P., CHUNG, D. & MARUSIC, I. 2012 Amplitude and frequency modulation in wall turbulence. *J. Fluid Mech.* **712**, 61–91.
- GUALA, M., HOMMEMA, S.E. & ADRIAN, R.J. 2006 Large-scale and very-large-scale motions in turbulent pipe flow. *J. Fluid Mech.* **554**, 521–542.
- GUBIAN, P.-A., STOKER, J., MEDVESCEK, J., MYDLARSKI, L. & BALIGA, B.R. 2019 Evolution of wall shear stress with Reynolds number in fully developed turbulent channel flow experiments. *Phys. Rev. Fluids* **4** (7), 074606.
- HANDLER, R.A., SAYLOR, J.R., LEIGHTON, R.I. & ROVELSTAD, A.L. 1999 Transport of a passive scalar at a shear-free boundary in fully developed turbulent open channel flow. *Phys. Fluids* **11** (9), 2607–2625.
- HANDLER, R.A., SWEAN JR, T.F., LEIGHTON, R.I. & SWEARINGEN, J.D. 1993 Length scales and the energy balance for turbulence near a free surface. *AIAA J.* **31** (11), 1998–2007.
- HOYAS, S., OBERLACK, M., ALCÁNTARA-ÁVILA, F., KRAHEBERGER, S.V. & LAUX, J. 2022 Wall turbulence at high friction Reynolds numbers. *Phys. Rev. Fluids* **7** (1), 014602.
- HUSSAIN, A.K.M.F. & REYNOLDS, W.C. 1975 Measurements in fully developed turbulent channel flow. *Trans. ASME J. Fluids Engng* **97** (4), 568–578.
- HUTCHINS, N. & MARUSIC, I. 2007 Evidence of very long meandering features in the logarithmic region of turbulent boundary layers. *J. Fluid Mech.* **579**, 1–28.
- JIMÉNEZ, J. 2012 Cascades in wall-bounded turbulence. *Annu. Rev. Fluid Mech.* **44**, 27–45.
- JIMÉNEZ, J. & MOSER, R.D. 2007 What are we learning from simulating wall turbulence? *Phil. Trans. R. Soc. A* **365** (1852), 715–732.
- KHOSRONEJAD, A. & SOTIROPOULOS, F. 2014 Numerical simulation of sand waves in a turbulent open channel flow. *J. Fluid Mech.* **753**, 150–216.

- KIM, K.C. & ADRIAN, R.J. 1999 Very large-scale motion in the outer layer. *Phys. Fluids* **11** (2), 417–422.
- KIM, J., MOIN, P. & MOSER, R. 1987 Turbulence statistics in fully developed channel flow at low Reynolds number. *J. Fluid Mech.* **177**, 133–166.
- KLEWICKI, J.C. 2022 Bounded dissipation predicts finite asymptotic state of near-wall turbulence. *J. Fluid Mech.* **940**, F1.
- KOMORI, S., NAGAOSA, R., MURAKAMI, Y., CHIBA, S., ISHII, K. & KUWAHARA, K. 1993 Direct numerical simulation of three-dimensional open-channel flow with zero-shear gas–liquid interface. *Phys. Fluids A* **5** (1), 115–125.
- LAM, K. & BANERJEE, S. 1992 On the condition of streak formation in a bounded turbulent flow. *Phys. Fluids A* **4** (2), 306–320.
- LEE, M., MALAYA, N. & MOSER, R.D. 2013 Petascale direct numerical simulation of turbulent channel flow on up to 786k cores. In *SC'13: Proceedings of the International Conference on High Performance Computing, Networking, Storage and Analysis*, pp. 1–11. ACM Press.
- LEE, M. & MOSER, R.D. 2015 Direct numerical simulation of turbulent channel flow up to  $Re = 5200$ . *J. Fluid Mech.* **774**, 395–415.
- LEE, M. & MOSER, R.D. 2019 Spectral analysis of the budget equation in turbulent channel flows at high Reynolds number. *J. Fluid Mech.* **860**, 886–938.
- LÓPEZ, F. & GARCÍA, M. 1998 Open-channel flow through simulated vegetation: suspended sediment transport modeling. *Water Resour. Res.* **34** (9), 2341–2352.
- LOZANO-DURÁN, A. & JIMÉNEZ, J. 2014 Effect of the computational domain on direct simulations of turbulent channels up to  $Re\tau = 4200$ . *Phys. Fluids* **26** (1), 011702.
- MARUSIC, I., BAARS, W.J. & HUTCHINS, N. 2017 Scaling of the streamwise turbulence intensity in the context of inner–outer interactions in wall turbulence. *Phys. Rev. Fluids* **2**, 100502.
- MARUSIC, I., MONTY, J.P., HULTMARK, M. & SMITS, A.J. 2013 On the logarithmic region in wall turbulence. *J. Fluid Mech.* **716**, R3.
- MATHIS, R., HUTCHINS, N. & MARUSIC, I. 2009 Large-scale amplitude modulation of the small-scale structures in turbulent boundary layers. *J. Fluid Mech.* **628**, 311–337.
- MONTY, J.P., HUTCHINS, N., NG, H.C.H., MARUSIC, I. & CHONG, M.S. 2009 A comparison of turbulent pipe, channel and boundary layer flows. *J. Fluid Mech.* **632**, 431–442.
- MORRISON, J.F., JIANG, W., MCKEON, B.J. & SMITS, A.J. 2002 Reynolds number dependence of streamwise velocity spectra in turbulent pipe flow. *Phys. Rev. Lett.* **88** (21), 214501.
- NAGIB, H.M. & CHAUHAN, K.A. 2008 Variations of von Kármán coefficient in canonical flows. *Phys. Fluids* **20** (10), 101518.
- NEZU, I. 2005 Open-channel flow turbulence and its research prospect in the 21st century. *ASCE J. Hydraul. Engng* **131** (4), 229–246.
- NEZU, I. & RODI, W. 1986 Open-channel flow measurements with a laser Doppler anemometer. *ASCE J. Hydraul. Engng* **112** (5), 335–355.
- PAN, Y. & BANERJEE, S. 1995 A numerical study of free-surface turbulence in channel flow. *Phys. Fluids* **7** (7), 1649–1664.
- PERUZZI, C., POGGI, D., RIDOLFI, L. & MANES, C. 2020 On the scaling of large-scale structures in smooth-bed turbulent open-channel flows. *J. Fluid Mech.* **889**, A1.
- PINELLI, M., HERLINA, H., WISSINK, J.G. & UHLMANN, M. 2022 Direct numerical simulation of turbulent mass transfer at the surface of an open channel flow. *J. Fluid Mech.* **933**, A49.
- QI, M., LI, J., CHEN, Q. & ZHANG, Q. 2018 Roughness effects on near-wall turbulence modelling for open-channel flows. *J. Hydraul. Res.* **56** (5), 648–661.
- RENARD, N. & DECK, S. 2016 A theoretical decomposition of mean skin friction generation into physical phenomena across the boundary layer. *J. Fluid Mech.* **790**, 339–367.
- ROUSSINOVA, V., SHINNEEB, A.-M. & BALACHANDAR, R. 2010 Investigation of fluid structures in a smooth open-channel flow using proper orthogonal decomposition. *ASCE J. Hydraul. Engng* **136** (3), 143–154.
- SAMIE, M., MARUSIC, I., HUTCHINS, N., FU, M.K., FAN, Y., HULTMARK, M. & SMITS, A.J. 2018 Fully resolved measurements of turbulent boundary layer flows up to  $Re\tau = 20\,000$ . *J. Fluid Mech.* **851**, 391–415.
- SCHLATTER, P. & ÖRLÜ, R. 2010 Quantifying the interaction between large and small scales in wall-bounded turbulent flows: a note of caution. *Phys. Fluids* **22** (5), 051704.
- SCHLATTER, P., LI, Q., BRETHOUWER, G., JOHANSSON, A.V. & HENNINGSON, D.S. 2010 Simulations of spatially evolving turbulent boundary layers up to  $Re\theta = 4300$ . *Intl J. Heat Fluid Flow* **31** (3), 251–261.
- SCHOPPA, W. & HUSSAIN, F. 2002 Coherent structure generation in near-wall turbulence. *J. Fluid Mech.* **453**, 57–108.
- SHE, Z.-S., CHEN, X. & HUSSAIN, F. 2017 Quantifying wall turbulence via a symmetry approach: a lie group theory. *J. Fluid Mech.* **827**, 322–356.



## DNS of open channel flows

- SWEAN, T. JR., LEIGHTON, R., HANDLER, R. & SWEARINGEN, J. 1991 Turbulence modeling near the free surface in an open channel flow. In *29th Aerospace Sciences Meeting*, p. 613. AIAA.
- TACHIE, M.F. & ADANE, K.K. 2007 PIV study of shallow open channel flow over d- and k-type transverse ribs. *Trans. ASME J. Fluids Engng* **129** (8), 1058–1072.
- TAMBURRINO, A. & GULLIVER, J.S. 1999 Large flow structures in a turbulent open channel flow. *J. Hydraul. Res.* **37** (3), 363–380.
- TARDU, S. 2017 Near wall dissipation revisited. *Intl J. Heat Fluid Flow* **67**, 104–115.
- TOWNSEND, A.A. 1976 *The Structure of Turbulent Shear Flow*. Cambridge University Press.
- WALEFFE, F. 1997 On a self-sustaining process in shear flows. *Phys. Fluids* **9** (4), 883–900.
- WANG, G. & RICHTER, D.H. 2019 Two mechanisms of modulation of very-large-scale motions by inertial particles in open channel flow. *J. Fluid Mech.* **868**, 538–559.
- WANG, H., ZHONG, Q., WANG, X. & LI, D. 2017 Quantitative characterization of streaky structures in open-channel flows. *ASCE J. Hydraul. Engng* **143** (10), 04017040.
- WU, W., RODI, W. & WENKA, T. 2000 3D numerical modeling of flow and sediment transport in open channels. *ASCE J. Hydraul. Engng* **126** (1), 4–15.
- YAO, J., CHEN, X. & HUSSAIN, F. 2019 Reynolds number effect on drag control via spanwise wall oscillation in turbulent channel flows. *Phys. Fluids* **31** (8), 085108.
- YOSHIMURA, H. & FUJITA, I. 2020 Investigation of free-surface dynamics in an open-channel flow. *J. Hydraul. Res.* **58** (2), 231–247.